https://doi.org/10.15407/ufm.25.01.027

D.O. KHARCHENKO[1,*], V.O. KHARCHENKO[1,2,], O.M. SHCHOKOTOVA[1,***], V.V. KUPRIIENKO[1], O.B. LYSENKO[1], and S.V. KOKHAN[1]**

[1] Institute of Applied Physics of the N.A.S. of Ukraine, 58 Petropavlivska Str., UA-40000 Sumy, Ukraine

[2] Sumy State University, 2 Rymskogo-Korsakova Str., UA-40007 Sumy, Ukraine

* dikh@ipfcentr.sumy.ua, ** vasiliy@ipfcentr.sumy.ua, *** shchokotova@gmail.com

MODELLING PRECIPITATION OF THE SECONDARY PHASE IN COMMERCIAL ZIRCONIUM ALLOYS AT NEUTRON IRRADIATION

The work deals with the study of secondary-phase precipitation in binary and ternary zirconium-based alloys with extra-small content of doping within the framework of the phase-field approach. Developed phase-field model is applied to study β-phase precipitation in the model system of commercial Zr–Nb–Sn and Zr–Nb alloys at thermal treatment. An analysis of local rearrangement of doping and equilibrium vacancies during precipitation is provided. Kinetics of precipitation, size and distribution of the precipitates, concentration of the species in precipitates and matrix are studied. Mechanical response including the plastic deformations in precipitated solid is discussed. As shown, the yield-strength change increases during precipitation. Yield and ultimate strength are studied at different shear rates for the annealed alloy. Formation and growth of slip planes and dislocation loop–precipitate interaction governed by elastic-moduli difference is analysed. As shown, the emergence of dislocation loops around precipitates follows the Orowan's mechanism. Modelling the radiation-induced precipitation during neutron irradiation of zirconium alloys with low content of doping is performed within the framework of the developed phase-field model by taking into account ballistic mixing and the

Citation: D.O. Kharchenko, V.O. Kharchenko, O.M. Shchokotova, V.V. Kupriienko, O.B. Lysenko, and S.V. Kokhan, Modelling Precipitation of the Secondary Phase in Commercial Zirconium Alloys at Neutron Irradiation, *Progress in Physics of Metals*, **25**, No. 1: 27–73 (2024)

dynamics of point defects with their sinks. As shown, in a sample initially containing precipitates of the secondary phase, irradiation results in the dissolution of precipitates at small doses and reprecipitation with dose accumulation. Analysis of precipitation dynamics and statistical distributions of precipitates with local rearrangement of non-equilibrium vacancies around precipitates at neutron irradiation is provided. As shown, the competition between the ballistic mixing and the thermodynamic force plays a major role in kinetics of radiation-induced precipitation and precipitates' dissolution. The estimation of mechanical properties of Zr–Nb alloy during irradiation under reactor conditions is provided.

Keywords: phase field, precipitation, neutron irradiation, defects, hardening.

1. Introduction

For several decades, zirconium-based alloys have been widely utilized as materials for the cladding of nuclear reactor fuel rods due to their low cross-section for thermal neutron absorption, adequate corrosion/hydriding resistance, acceptable plasticity, and high strength. The improved properties of these alloys are attributed to microstructural features associated with the presence of niobium. The precipitation of the β-Nb phase with a body-centred cubic crystalline structure in the α-Zr matrix, characterized by a hexagonal crystalline structure with close packing, leads to enhanced corrosion and hydriding resistance [1–5]. It has been demonstrated that the addition of niobium to zirconium alloys can play a crucial role in solid-phase solubility to extend the claddings' service life [6].

In commercial alloys modified with niobium and used in research and industrial reactors, such as ZIRLO, Zr–1% Nb, and Zr–2.5% Nb, the concentration of added niobium varies from 1 to 3 wt.%, in contrast to the low concentration of other traditional elements (Sn, Fe, Cr, Ni) added to improve the physical, mechanical, and corrosion properties of cladding materials. It has been demonstrated that the precipitation of niobium strongly depends on the additional alloying elements due to its high chemical reactivity. The size of β-Nb precipitates is influenced by the content of additional elements, annealing temperature, and manufacturing technology. Experimental data on niobium precipitate statistics show precipitate size (diameter) values in the range of 13–57 nm with a density of $(1–4)\times 10^{14}$ cm^{-3} at temperatures between 573–873 K and varying levels of additional alloying [7–14]. The corrosion of zirconium is inhibited by the presence of a high density of nanoscale precipitates [15–20]. Tin is added to enhance material strength and creep resistance, reducing zirconium corrosion [21].

Theoretical studies of zirconium alloys alloyed with lead and niobium reveal that lead atoms tend to dissolve in the α-Zr matrix, localizing vacancies, while niobium atoms form β-phase clusters and exhibit a repulsive interaction with vacancies [22, 23]. In this case, a study of the

local concentration rearrangement of these two types of atoms and vacancies in systems with very low content of alloying elements becomes challenging when stable-sized precipitates are formed. As known, precipitates act as obstacles for dislocations, leading to an increase in the materials' yield strength. The β-Nb precipitates generate local elastic stresses that determine changes in strength under mechanical loads and influence the formation of slip planes during deformation. Studying the evolution of the defect structure around such precipitates provides further insight into the interaction features between precipitates and defects under external loads.

Overall, the study of the local rearrangement of alloying elements remains a relevant issue for multicomponent alloys, where the precipitation of secondary phases affects the physical and mechanical properties of these alloys. Earlier studies have shown that due to the strong interaction between precipitates and dislocations, closely distributed precipitates significantly improve mechanical properties by Orowan's strengthening [24]. The separated phase can increase yield strength and strength while reducing material ductility [25]. The matrix–precipitate interphase boundary induces martensitic transformation [26]. Significant progress in the theoretical study of these effects has been made based on the classical approaches developed by Cahn and Hilliard [27–31] generalized into the phase-field theory [32–37].

Additionally, predicting the behaviour of materials under extreme conditions remains a pressing issue in nuclear energy (for extending reactor service life, ensuring safety in operation, and developing new structural materials for reactors) and aerospace science (developing materials with the best performance in aggressive environments). It is well-known that under non-equilibrium conditions in materials, especially when subjected to high-energy particle irradiation, phenomena of self-organization occur. These phenomena include the dissolution and precipitation of precipitates, growth and/or amorphization of precipitates, segregation processes, phase transformations, redistribution of alloying elements, formation of packing defects, and dislocation loops, all of which lead to changes in the physical and mechanical properties of the material [12, 38].

In the study of zirconium-based alloys, it has been observed that during irradiation, the flow of point defects accelerates the diffusion of alloying elements (Nb at 1–3 at.%, while Sn, Fe, Cr, Cu are less than 1 at.%). This leads to the formation of numerous new precipitates [39–43]. Detailed experimental and numerical investigations have shown that the size of β-precipitates (with > 80% niobium content) that appear in the α-Zr matrix after an incubation dose of about 1 displacement per atom (dpa) [44], and their density, depend on irradiation conditions [12, 14, 45], while large spherical precipitates are less affected by irradia-

tion [46]. Non-equilibrium defects generated during irradiation migrate under the influence of forces determined by gradients of chemical potential and elastic interactions, leading to radiation-induced segregation, precipitation of precipitates, and the formation of dislocation loops. These factors collectively affect the materials' performance in reactors [12, 38, 45].

Understanding microstructural transformations in such alloys enables the development of recommendations regarding the use of existing materials for fuel rod cladding or the development of new materials. In this context, the problem of phase stability in unirradiated samples, pre-irradiated samples, and structural components under irradiation remains relevant [47]. It is known that atomic displacement cascades lead to the dissolution of existing precipitates and the formation of new ones. In such cases, reprecipitation of precipitates can occur, resulting in a new microstructure composed of existing and newly formed precipitates. On the other hand, new precipitates can form from a diluted solution in the matrix due to ballistic mixing of atoms. Both of these phenomena regulate the material's behaviour under irradiation and the alteration of its mechanical and physical properties.

Typically, experimental studies of the aforementioned phenomena in fuel rod claddings take several years in reactor conditions and are a costly procedure. An alternative approach involves utilizing multiscale computer modelling with various methods for analysing material properties, ranging from quantum mechanics to statistical thermodynamics. One of the most powerful tools in this procedure is phase-field modelling, which allows the observation of the spatial rearrangement of alloying elements and the transformation of the defect microstructure under various irradiation conditions [48].

The phase-field approach includes thermodynamic potentials of the alloys' components and the concentration of point defects [32–35, 49]. It is widely employed in the study of phase transformations in binary and multicomponent alloys during heat treatment with local component rearrangement and defects [33, 50, 51]. It is also used for investigating radiation damage and microstructure evolution in various materials [50–57]. This method has been applied to determine mechanical responses to external loads [57, 58] and investigate martensitic transformations [59, 60]. For the study of microstructural transformations, the CALPHAD method is used in combination with realistic thermodynamic potentials [61, 62]. This, coupled with reaction rate theory for the evolution of point defects, enables the examination of localized defect rearrangements [53, 57], their clusters [48], dislocation loops [63], pores [50, 52, 64], and the formation/dissolution of secondary phases [36]. Modelling using the phase-field method for Zr–Nb alloys during heat treatment has been discussed in works [37, 65]. Radiation-induced pre-

cipitation has been studied for zirconium alloys with an elevated niobium concentration [51, 57].

Usually, when employing the phase-field method, one operates with the spatial–temporal evolution of alloying element concentrations. In the corresponding numerical procedures, various calculation methods can be used, such as finite difference methods, Fourier transform methods, and finite element procedures (see, for example, Ref. [66] and the references therein).

Most studies that use the phase-field method to model microstructural transformations are performed for alloys with high contents of major alloying elements (>10%). However, in commercial zirconium alloys, the alloying content can be less than 1%. Therefore, when modelling systems with extremely low concentrations of alloying elements during thermal processing and irradiation using the phase-field method, computational challenges arise. These challenges are associated with handling the entropy part of the thermodynamic potential, which assumes extremely low values compared to other parts of this potential, leading to computational scheme divergence.

This work employs a method to overcome the aforementioned computational problems for systems with low alloying element content (specifically, less than 1%). This allows for modelling the precipitation of secondary phases in commercial zirconium alloys. It begins by examining the precipitation process in the Zr–1%Nb-1%Sn ternary alloy, which serves as a prototype for the commercial ZIRLO alloy. The local reordering of alloying elements and vacancies during the heat treatment of the solid solution is investigated. A phase-field model using CALPHAD potentials [61, 62] is developed to provide a more realistic description of the studied method is combined with reaction rate theory, taking into account ballistic mixing and the dynamics of point defects and their sinks.

The novelty of this research lies in studying the local redistribution of tin and vacancies during the precipitation of the β-phase during heat treatment, resulting in changes in strength and mechanical response to external loading. This is regulated by dislocation-precipitate interactions in the prototype model of commercial zirconium-based alloys. The dynamics and statistical properties of β-phase precipitates are examined, along with the mechanical properties of the annealed alloy at different deformation rates. The dynamics of dislocation loops are discussed, and the evolution of dislocation loops near niobium precipitates is analysed to understand the impact of solid domains and interfacial boundaries on the distribution of elastic fields, which regulate dislocation motion.

The study further explores two competing mechanisms that determine the dissolution of precipitates and radiation-induced precipitation in the binary Zr–2%Nb alloy under neutron irradiation. This helps establish the details of radiation-induced dissolution and precipitation of

precipitates. The results obtained are used to assess changes in the mechanical properties of the material under reactor conditions. Additionally, this study investigates primary and radiation-induced reprecipitation in the dissolved Zr–2%Nb–0.5%Sn alloy, as well as radiation-induced niobium precipitation within the matrix phase containing 0.4% niobium. It will be demonstrated that the modelling results align well with experimental observations.

The structure of the work is as follows. In Section 2, the phase field model for investigating precipitate formation during heat treatment and irradiation, considering the dynamics of point defect sinks, is described. Section 3 presents the results of the modelling work. Subsection 3.1 provides results for the precipitation process in the Zr–1%Nb–1%Sn ternary alloy with a statistical analysis. It discusses the dynamics of the yield strength of precipitates and models shear deformation at different deformation rates. The obtained deformation curves are discussed, taking into account the dynamics of dislocation loops and the 'dislocation loop–precipitate' interaction. The evolution of stress distribution in a sheared and compressed sample and the local stress redistribution around the precipitate during dislocation loop formation are investigated. Subsection 3.2 discusses the results of modelling for the binary Zr–2%Nb alloy during different stages of heat treatment and irradiation. Dose dependences of the measured average precipitate size, the density of precipitates, the density of dislocation loops, and strengthening under irradiation are discussed. In Subsection 3.3, the results of modelling radiation-induced formation of nanosized β-Nb particles in the matrix of the α-Zr solid solution of the Zr–2%Nb–0.5%Sn alloy are presented. The redistribution of tin atoms and out-of-equilibrium vacancies (based on their local concentrations) around precipitates is discussed. The dynamics of the average precipitate size and their number density are analysed. Section 4 summarizes the main conclusions of the research.

Overall, the research appears to be a comprehensive exploration of precipitate formation and evolution in zirconium-based alloys during thermal treatments and irradiation, with a focus on the structural and mechanical properties of these materials under extreme conditions. The phase field modelling approach provides insights into the behaviour of these alloys, even with very low alloying element concentrations, and offers valuable information for practical applications in nuclear reactors and other extreme environments.

2. Phase-Field Model

In this section, a phase-field model for investigating precipitate formation during annealing and irradiation in zirconium–niobium (Zr–Nb) and zirconium–niobium–tin (Zr–Nb–Sn) alloys is presented, utilizing

the CALPHAD method combined with reaction rate theory. Subsection 2.1 outlines the model for microstructural transformations with precipitate formation during thermal processing. The modelling approach for radiation-induced transformations during neutron irradiation is discussed in subsection 2.2. The model used in this work is based on the assumptions and findings discussed in prior studies [37, 51, 57, 65], the principles of reaction rate theory [67–69], and investigations into radiation-induced ballistic mixing [70–74].

2.1. Thermodynamic Model of the System at Equilibrium Conditions

As known, the crystal structure of β-precipitates differs from the matrix structure of zirconium. Furthermore, in the real Zr–Nb system, the matrix–precipitate interfacial boundary is incoherent. Typically, to describe structural transformations, an order parameter (phase field) is introduced to account for this phase difference. To describe the incoherent interfacial boundary, we incorporate a dislocation density into the corresponding phase-field model. In our recent work [51], we employed this combined phase-field approach, which allows distinguishing β-phase precipitates from the α-Zr matrix with vacancy segregation around the incoherent interfacial boundary. It was demonstrated that the phase field adheres to the spatial distribution of niobium concentration when all the niobium-enriched domains belong to the β-phase. This makes it possible to recognize that phase separation, resulting in the formation of a niobium-enriched phase solely in β-Nb and the α-Zr phase, can only be described through the concentration field.

In this study, to describe binary Zr–Nb and ternary Zr–Nb–Sn alloys, we operate with atomic concentrations of zirconium and alloying elements as continuous fields evolving in both space (**r**) and time (t). These fields are denoted as $c_\mu(\mathbf{r}, t) = N_\mu(\mathbf{r}, t)/N$ for $\mu = \{\text{Zr, Nb}\}$ in the case of a binary alloy and $\mu = \{\text{Zr, Nb, Sn}\}$ for the ternary alloy, where $N_\mu(\mathbf{r}, t)$ represents the number of atoms of species μ, and N is the total number of atoms. The vacancy subsystem is described by the concentration $c_v(\mathbf{r}, t) = N_v(\mathbf{r}, t)/N$. In the case of the ternary alloy, we consider that tin atoms act as traps for vacancies. Interstitial atoms are not explicitly represented since they have low concentrations compared to vacancies. Additionally, by assuming that the diffusion of alloying element atoms occurs primarily through the vacancy mechanism, the contribution of interstitials to the thermodynamics can be neglected. The system is considered in a fixed volume V, and it adheres to the conservation of mass law, *i.e.*, $\sum_\mu c_\mu = 1$.

The total Gibbs energy of the studied system is expressed as the sum of all components associated with the thermodynamics of the system [61]: $G_{tot} = G_c + G_v$, where G_c relates to the alloy properties, G_v corre-

sponds to the vacancy subsystem. The molar Gibbs energy of the alloy is given by $G_c = G^{ref} + G^{id} + G^{ex}$, where $G^{ref} = \sum_\mu G_\mu^{0*} c_\mu$ represents the reference Gibbs energy, $G^{id} = RT\sum_\mu c_\mu \ln c_\mu$ accounts for random atomic mixing (R is the gas constant, and T is the temperature), $G^{ex} = c_\mu c_{\mu'} L_{\mu,\mu'}$ reflects deviations from idealness. For the binary Zr–Nb alloy, we have $G^{ex} = c_{Zr} c_{Nb} L_{Zr,Nb}$. In our approach, the reference energies G_{Zr}^{0*}, G_{Nb}^{0*}, and G_{Sn}^{0} are taken for pure α-Zr, β-Nb, and tin in the α-Zr phase, respectively, based on SGTE (Scientific Group Thermodata Europe) data [62]. $L_{\mu,\mu'} = \sum_n (c_\mu - c_{\mu'})^n L^n_{\mu,\mu'}(T)$, where $L^n_{\mu,\mu'}(T)$ are temperature-dependent coefficients.

The contribution of the vacancy subsystem G_υ can be expressed as follows:

$$G_\upsilon = G_\upsilon^f + G_\upsilon^{id} + G_\upsilon^{int}, \tag{1}$$

where the formation energy of vacancies G_υ^f is determined by

$$G_\upsilon^f = c_\upsilon \sum\nolimits_\mu G_\upsilon^{f,\mu} c_\mu . \tag{2}$$

Here, $G_\upsilon^{f,\mu}$ represents the formation energy of vacancies in pure materials. The corresponding entropy contribution is $G_\upsilon^{id} = RTc_\upsilon \ln c_\upsilon$. The term G_υ^{int} describes the interaction of vacancies with atoms of the alloy components and can be determined using the Gibbs energy components [38]:

$$G_\upsilon^{int} = c_\upsilon \sum\nolimits_\mu G_{\upsilon-\mu}^{int} c_\mu , \tag{3}$$

Here, for the vacancy–atom interaction energies, we use

$$G_{\upsilon-\mu}^{int} = \frac{G_{coh}^\mu + G_\upsilon^{f,\mu}}{Z} . \tag{4}$$

Here, G_{coh}^μ relates to cohesive energy, $Z = 12$ is the coordination number. In this case, the full expression for the Gibbs energy $G_{tot}(\{c_\mu\}, c_\upsilon)$ of the ternary Zr–Nb–Sn alloy is given as follows:

$$\begin{aligned} G_{tot}\left(\{c_{Zr}, c_{Nb}, c_{Sn}\}, c_\upsilon\right) = G_{Zr}^{0*} c_{Zr} + G_{Nb}^{0*} c_{Nb} + G_{Sn}^{0*} c_{Sn} + \\ + RT\left[c_{Zr} \ln c_{Zr} + c_{Nb} \ln c_{Nb} + c_{Sn} \ln c_{Sn} + c_\upsilon \ln c_\upsilon\right] + \\ + c_{Zr} c_{Nb} L_{Zr,Nb}^0 + c_{Zr} c_{Sn} L_{Zr,Sn}^0 + c_{Nb} c_{Sn} L_{Nb,Sn}^0 + \\ + \left(\left[G_\upsilon^{f,Zr} + G_{\upsilon-Zr}^{int}\right] c_{Zr} + \left[G_\upsilon^{f,Nb} + G_{\upsilon-Nb}^{int}\right] c_{Nb} + \left[G_\upsilon^{f,Sn} + G_{\upsilon-Sn}^{int}\right] c_{Sn}\right) c_\upsilon . \end{aligned} \tag{5}$$

Using the model of smooth interphase diffusion, we represent the corresponding Gibbs energy functional as:

$$\mathcal{G} = \frac{1}{V_m} \int \mathrm{d}V \left[G_{tot}\left(\{c_\mu\}, c_\upsilon\right) + \sum_\mu \kappa_\mu \left(\nabla c_\mu\right)^2 + \kappa_\upsilon \left(\nabla c_\upsilon\right)^2 \right], \tag{6}$$

which includes the gradient terms κ_μ and κ_υ; here, V_m is the molar volume. Following the standard procedure [29], we further assume $\kappa_\mu = L^0_{Zr,Nb} l^2/6$, where $l = \delta_0/2$ is the coherence width, and δ_0 is the width of the interphase boundary. Without loss of generality, we can set $\kappa_\mu = \kappa_\upsilon = \kappa$.

In the case of the binary alloy, we apply the full Gibbs free energy functional in the following form:

$$\mathcal{G}' = \mathcal{G} + \int \frac{V_m \eta^2 E}{1-\upsilon} \left(c_{Zr} - \overline{c}\right)^2 \mathrm{d}V, \tag{7}$$

where the second term accounts for the deformation energy effect caused by the difference in compositions of the two phases, E is the elastic modulus, υ is the Poisson's ratio, η is the lattice parameter expansion coefficient, and a, $\overline{c} = 0.98$ is the average composition value.

From a formal point of view, the dynamics of the system should satisfy the Cahn–Hilliard continuity equations, which is given as $\partial_t c_\mu = \nabla \sum_{\mu'} M_{\mu,\mu'} \nabla \delta G / \delta c_{\mu'}$, where $M_{\mu,\mu'}$ represents the respective mobility. It is worth noting that for a system with an extremely low concentration of alloying elements, the chemical potentials $\delta G / \delta c_\mu$ diverge when $c_\mu << 1$ due to the corresponding entropy term. However, the chemical potential for zirconium does not diverge within the practical range of c_{Zr} (up to 20% niobium is dissolved in the matrix, niobium precipitates contain up to 80% niobium, and tin in the ternary alloy is dissolved in the matrix). Linear stability analysis shows that this divergence suppresses all possible spatial instabilities, leading to the non-physical result of system homogenization. To avoid this problem and realistically describe the precipitation of β-Nb precipitates in Zr–Nb and Zr–Nb–Sn alloys with low levels of alloying elements, it is possible to consider only the dynamics of the c_{Zr} field in the Zr–Nb alloy and the c_{Zr} and c_{Sn} fields in the Zr–Nb–Sn alloy (in combination with the c_υ dynamics) and calculate the c_{Nb} field from the mass conservation law. In this case, the law of mass conservation is not violated, and the niobium concentration values are obtained dynamically. This approach allows modelling phase separation processes at extremely low levels of alloying elements, avoiding the mentioned divergence in the chemical potential in the Cahn–Hilliard equation for $c_{Zr,Sn}(\mathbf{r}, t)$. This approach has been successfully used to study the precipitation of niobium precipitates in the binary Zr–Nb alloy and the ternary Zr–Nb–Sn alloy [75, 76, 77].

Following the standard phase-field approach for phase separation in ternary systems, we adopt the Onsager diffusion equations proposed by Khachaturyan [30]. Using the formalism derived earlier, as described in the works [78–81], we obtain the following system of coupled nonlinear equations that includes all diffusion flows from all components, as shown in work [82]:

$$\partial_t c_{Zr} = \nabla \cdot \left[M_{Zr,Zr} \nabla \frac{\delta \mathcal{G}}{\delta c_{Zr}} + M_{Zr,Sn} \nabla \frac{\delta \mathcal{G}}{\delta c_{Sn}} \right],$$

$$\partial_t c_{Sn} = \nabla \cdot \left[M_{Sn,Sn} \nabla \frac{\delta \mathcal{G}}{\delta c_{Sn}} + M_{Zr,Sn} \nabla \frac{\delta \mathcal{G}}{\delta c_{Zr}} \right],$$

$$\partial_t c_v = \nabla \cdot M_v \nabla \frac{\delta \mathcal{G}}{\delta c_v}. \tag{8}$$

For the considered class of alloys, we employ model assumptions for concentration-dependent mobilities based on previous works. This approach allows for a detailed investigation of the transient dynamics of the phase separation process and can have a significant impact on coarsening kinetics. The coefficients of chemical mobilities $M_{\mathrm{Zr,Zr}}$, $M_{\mathrm{Sn,Sn}}$, and $M_{\mathrm{Zr,Sn}}$ are determined as follows [82, 83]:

$$\begin{aligned}
M_{\mathrm{Zr,Zr}} &= c_{\mathrm{Zr}}\left[(1-c_{\mathrm{Zr}})^2 M_{\mathrm{Zr}} + c_{\mathrm{Zr}}c_{\mathrm{Sn}}M_{\mathrm{Sn}} + c_{\mathrm{Zr}}c_{\mathrm{Nb}}M_{\mathrm{Nb}}\right],\\
M_{\mathrm{Sn,Sn}} &= c_{\mathrm{Sn}}\left[(1-c_{\mathrm{Sn}})^2 M_{\mathrm{Sn}} + c_{\mathrm{Sn}}c_{\mathrm{Zr}}M_{\mathrm{Sn}} + c_{\mathrm{Sn}}c_{\mathrm{Nb}}M_{\mathrm{Nb}}\right],\\
M_{\mathrm{Zr,Sn}} &= c_{\mathrm{Zr}}c_{\mathrm{Sn}}\left[c_{\mathrm{Nb}}M_{\mathrm{Nb}} - (1-c_{\mathrm{Zr}})M_{\mathrm{Zr}} - (1-c_{\mathrm{Sn}})M_{\mathrm{Sn}}\right],
\end{aligned} \tag{9}$$

where $M_\mu = V_m D_\mu / RT$ is the mobility of the pure element, D_μ is the corresponding diffusion coefficient. Mobility for the vacancy ensemble is determined in the standard manner through the vacancy diffusion coefficient: $M_v = V_m D_v c_v / RT$.

2.2. Modelling Irradiation Influence

The presented thermodynamic formalism is applicable to systems in equilibrium, where the defect concentrations are close to their equilibrium values. When considering a system subjected to neutron irradiation, we account for the fact that the concentration of point defects significantly exceeds their equilibrium values by several orders of magnitude. This leads to radiation-enhanced diffusion of atoms $\tilde{D}_\mu = D_\mu + D_v\langle c_v\rangle + D_i\langle c_i\rangle$, where D_μ is the diffusion coefficient of atoms, $\langle c_v\rangle$ and $\langle c_i\rangle$ are the average concentrations of out-of-equilibrium vacancies and interstitials, respectively, and, $D_{v,i}$ are their respective diffusion coefficients [38]. Assuming $D_i c_i \approx D_v c_v$, we obtain the expression $\tilde{D}_\mu = D_\mu + 2D_v\langle c_v\rangle$ [84]. When considering atomic ballistic mixing induced by irradiation [70–74], the dynamics of the atomic subsystem are governed by equations of the form $\partial_t c_\mu = (\partial_t c_\mu)^{th} + (\partial_t c_\mu)^{bal}$. Here, the term $(\partial_t c_\mu)^{th} = -\nabla\cdot\mathbf{J}_c$ corresponds to thermodynamic fluxes, which, in the case of the ternary alloy, are described by the first and second equations of the system (8). Therefore, for the Zr–Nb–Sn alloy, we have:

$$\mathbf{J}_c = -\left[M_{\mu,\mu}\nabla\frac{\delta\mathcal{G}}{\delta c_\mu} + M_{\mu,\mu'}\nabla\frac{\delta\mathcal{G}}{\delta c_{\mu'}}\right], \tag{10}$$

where $M_{\mu,\mu}$ and $M_{\mu,\mu'}$ are denoted in Eq. (9). For binary alloy Zr–Nb, one has:

$$\mathbf{J}_c = -L_{\mathrm{Zr}}\nabla\frac{\delta\mathcal{G}}{\delta c_{\mathrm{Zr}}}, \tag{11}$$

where $L_{\mathrm{Zr}} = c_{\mathrm{Zr}}(1 - c_{\mathrm{Zr}})[(1 - c_{\mathrm{Zr}})\tilde{D}_{\mathrm{Zr}} + c_{\mathrm{Zr}}\tilde{D}_{\mathrm{Nb}}]/(RT)$ is the corresponding kinetic coefficient [85]. The term $(\partial_t c_\mu)^{bal} = \Gamma(\langle c_\mu \rangle_w - c_\mu)$ describes radiation induced structural disorder (ballistic mixing of atoms), here the average is taken over a distribution $w(\mathbf{r})$, related to ballistic exchange at irradiation [70–74]: $\langle c_\mu \rangle_w \equiv \int w(\mathbf{r} - \mathbf{r}')c_\mu(\mathbf{r}')d\mathbf{r}'$, where $w(r) = [2\pi R_0^2]^{-1}\exp(-r/R_0)$ relates to Yukawa-like potential, R_0 is the mean atomic relocation distance [74]. The atomic jump frequency is given by $\Gamma = KA_{irr}$, where K is the dose rate calculated according to the NRT standard [86], and $A_{irr} = 50$ for neutron irradiation [87].

Let us consider the subsystem of non-equilibrium defects. Generally, the dynamics of the point defects' concentrations are governed by equations of the form $\partial_t c_d = -\nabla \mathbf{J}_d + R_d(c_i, c_v; \rho_i, \rho_v)$, where $\mathbf{J}_d$ corresponds to the diffusional flux of d-type defects ($d = \{i, v\}$), and R_d represents the reaction part involving the formation, annihilation, and recombination of defects. For the latter, we can write: $R_d = K_d - D_d k_d^2(\rho_i, \rho_v)c_d - \alpha_r c_i c_v$, where $K_d = K(1 - \varepsilon_r)(1 - \varepsilon^s{}_d - \varepsilon^g{}_d)$ denotes the defect generation rates, ε_r is the efficiency of cascade recombination, and, $\varepsilon^s{}_d$ and $\varepsilon^g{}_d$ represent the efficiencies of defect clustering (the superscripts s and g correspond to sessile and glissade clusters). For the intensities of vacancies and interstitials sinks, we have $k_d^2(\rho_i, \rho_v) = Z_d{}^N\rho_N + Z_d{}^I\rho_I + Z_d{}^V\rho_V + Z_p\langle R_p \rangle N_p$, where ρ_N is the dislocation density, ρ_d represents the density of interstitial and vacancy loops, $\langle R_p \rangle$ and N_p are the average size and number density of precipitates, respectively. Consider that interstitial loops are $\langle a \rangle$-type loops (with the Burgers vector $1/3\langle 11\bar{2}0 \rangle$), and vacancy loops are $\langle c \rangle$-type loops (with the Burgers vector $1/6\langle 20\bar{2}3 \rangle$). The preference factors that determine the preference for defect absorption by the sinks are as follows: $Z_i^N = Z_i^I = Z_i^V = 1.1$, $Z_v^N = Z_v^I = Z_v^V = 1.0$, $Z_p = 4\pi$. The $\alpha_r = 4\pi r_{iv} D_i/\Omega_0$ relates to the recombination rate, where $r_{iv} = (2–3)a$ is the recombination radius of the defect, and, Ω_0 is the atomic volume.

The diffusion flux of vacancies takes the form $\mathbf{J}_v = \mathbf{J}_v^{th} + \mathbf{J}_v^{int}$, where $\mathbf{J}_v^{th} = -M_v\nabla(\delta\Gamma/\delta c_v)$ represents the thermodynamic flux due to concentration gradients, and, $\mathbf{J}_v^{int} = M_v E V_m/3(1 - 2\upsilon)\nabla(1 + r_{v0}^2(1 + \upsilon)/[3(1 - \upsilon)]\nabla^2)c_v$ accounts for vacancy-vacancy interactions through lattice strain [51, 53, 57, 88, 89]. Here, $r_{v0} \approx (2–3)a$ denotes the root-mean-square distance between the defect and a matrix atom. In this model, it is assumed that interstitial atoms are uniformly distributed throughout the system. Additionally, considering the relationship $D_i >> D_v$, leading to the fast migration of interstitials to their sinks (dislocation networks, dislocation loops, precipitates, and grain boundaries) in comparison to vacancies, we can approximate $\partial_t c_i \approx 0$. This allows us to express $c_i = {}_{K_i}/(D_i k_i^2(\rho_i, \rho_v) + \alpha_r c_v)$. Following the approach extensively discussed in Ref. [51], in a simplified case, you can set

$$\mathcal{R}_v(c_v;\rho_i,\rho_v) \approx \mathcal{K}_v - \left[D_v k_v^2(\rho_i,\rho_v) + \frac{\alpha_r \mathcal{K}_i}{D_i k_i^2(\rho_i,\rho_v) + \alpha_r c_v} \right] c_v . \quad (12)$$

Thus, the dynamic equations for the system under irradiation take the following form:

$$\partial_t c_\mu = \Gamma(\langle c_\mu \rangle_w - c_\mu) - \nabla \cdot \mathbf{J}_c ; \quad (13)$$

$$\partial_t c_v = \mathcal{R}_v(c_v;\rho_i,\rho_v) - \nabla \cdot \mathbf{J}_v . \quad (14)$$

It is important to consider the growth of dislocation loops during irradiation, which leads to an increase in the intensity of sinks as the dose accumulates. Focusing our study on the kinetics of precipitate nucleation, we continue to use the simplified model while adhering to the approach described in works [67–69] and applying the formalism presented in the paper [51]. In this case, the dynamics of the radii of interstitial and vacancy loops, $R_i = R_i^m$ and R_v (where $m = \{a_1, a_2, a_3\}$ represents crystallographic directions), can be described by the equations:

$$b_a \partial_t R_i = Z_i^I D_i \langle c_i \rangle - Z_v^I D_v \left(\langle c_v \rangle - c_{iL} \right) + \frac{\mathcal{K}\varepsilon_{ig}}{3(\rho_N + \rho_i/3)} - \frac{b_a R_i}{2N_i} \partial_t N_i , \quad (15)$$

$$b_c \partial_t R_v = Z_v^V D_v \left(\langle c_v \rangle - c_{vL} \right) - Z_i^V D_i \langle c_i \rangle + \frac{\mathcal{K}\varepsilon_{vg}}{3(\rho_N + \rho_v)} - \frac{b_c R_v}{2N_v} \partial_t N_v . \quad (16)$$

Here, $b_{a,c}$ represents the values of the corresponding Burgers vector, $\langle c_i \rangle$ is calculated from $\langle c_v \rangle$ directly, $c_{i,vL}$ relates to the equilibrium vacancy concentration near vacancy/interstitial loops [67]. Loop densities, $\rho_I = \Sigma_m 2\pi R_i^m N_i^m$ and $\rho_V = 2\pi R_v N_v$ are determined by the dynamics of the number density of interstitial and vacancy loops, $N_i = N_i^m$ and N_v, satisfying equations of the form [68]:

$$\partial_t N_i = \begin{cases} \dfrac{K N_i^{max}}{3\phi_{max}}, & N_i \le N_i^{max}/3, \\ 0, & N_i > N_i^{max}/3; \end{cases} \quad (17)$$

$$\partial_t N_v = \begin{cases} 0, & \phi < \phi_c, \\ \dfrac{K N_v^{max} A \exp\left(\dfrac{A(\phi - \phi_c)}{\phi_{max} - \phi_c} \right)}{(\phi_{max} - \phi_c)\left[\exp(A) - 1\right]}, & \phi \ge \phi_c, \quad N_v < N_v^{max}, \\ 0, & \phi \ge \phi_c, \quad N_v \ge N_v^{max}. \end{cases} \quad (18)$$

The parameters used in simulations

Paramete r	Value	Dimen-sion	Refs.
Lattice parameters (a, c)	$(3.2; 5.14)\cdot 10^{-8}$	cm	
Atomic volume (Ω)	$3.32\cdot 10^{-23}$	cm^3	
Equilibrium vacancy concentration (c_{v0})	$0.54e^{-G_v^{f,\mathrm{Zr}}/k_BT}$	at. frac.	[84]
Vacancy formation energy ($G_v^{f,\mathrm{Zr}}$)	1.8	eV	[84]
Vacancy formation energy ($G_v^{f,\mathrm{Nb}}$)	2.7	eV	[95]
Vacancy formation energy ($G_v^{f,\mathrm{Sn}}$)	0.94	eV	[23]
Cohesive energy (G_{coh}^{Zr})	6.3	eV	[95]
Cohesive energy (G_{coh}^{Nb})	7.5	eV	[95]
Cohesive energy (G_{coh}^{Sn})	3.15	eV	[96]
Reference Gibbs energy (G_{Zr}^{0*})	$-7829 + 125.649T - 241618T\ln T - 0.00437791T^2 - 34971/T$	J/mole	[62]
Reference Gibbs energy (G_{Nb}^{0*})	$-8519.35 + 142.048T - 26.4711T\ln T - 0.000203475T^2 + 3.50119\cdot 10^{-7}T^3 + 93398/T$	J/mole	[62]
Reference Gibbs energy (G_{Sn}^{0*})	$6424.724 - 0.394731T - 8.2590486T\ln T - 0.016814429T^2 + 0.2623131\cdot 10^{-5}T^3 - 1081244/T - 0.12307\cdot 10^{26}/T^{-9}$	J/mole	[62]
Interaction parameter ($L^0_{\mathrm{Zr,Nb}}$)	$15911 + 3.35T$	J/mole	[62]
Interaction parameter ($L^0_{\mathrm{Zr,Sn}}$)	$-148022.5 + 19.4074T$	J/mole	[62]
Interaction parameter ($L^0_{\mathrm{Nb,Sn}}$)	15439.95	J/mole	[62]
Bulk modulus (K_{Zr})	97	GPa	[97–99]
Bulk modulus (K_{Nb})	170	GPa	[97, 99, 100]
Bulk modulus (K_{Sn})	58	GPa	[101]
Poisson ratio (υ)	0.34		[102]
Young modulus (E)	98.8	GPa	
Interface width (δ)	5	Nm	[37]
Diffusivity of Nb in α-Zr (D_{Nb})	$6.6\cdot 10^{-10}e^{-15851.4/T}$	m^2/s	[37]
Diffusivity of Sn in α-Zr (D_{Sn})	$3.12\cdot 10^{-6}e^{-2.74\ \mathrm{eV}/k_BT}$	m^2/s	[103]
Vacancy diffusivity (D_v)	$2.2\cdot 10^{-2}e^{-0.93\ \mathrm{eV}/k_BT}$	cm^2/s	[104]
Interstitial diffusivity (D_i)	$3.5\cdot 10^{-4}e^{-0.06\ \mathrm{eV}/k_BT}$	cm^2/s	[104]
Expansion coefficient (h)	0.045		
Clusterization efficiencies (ε_r, ε_i^s, ε_i^g, ε_v^s, ε_v^g)	0.95; 0.5; 0.17; 0.65; 0.05		[51]
Fitting parameter (A)	5.0		[68]
Fitting parameter (φ_{max})	3.86	dpa	[68]

Here, we use experimental data on loop nucleation [10, 90–92]: interstitial loops are formed from the beginning of irradiation and reach typical values of $N_{i,v}^{max} \sim 10^{16}$ cm^{-3}, while vacancy loops nucleate at doses above the critical $\varphi_c = 3$ dpa and after reaching a density of $N_v^{max} \sim 10^{15}$ cm^{-3}; A and φ_{max} are fitting parameters [68]. All the parameters used in the modelling are summarized in Table 1.

Thus, the overall dynamics of the system under irradiation is described by the set of equations (13)–(18). For numerical calculations, the following rescalings are used: $r' = r/l$, $t' = tD_v/l^2$. To ensure computational accuracy when solving the dynamic equations, a Fourier spectral method is employed on a cubic grid of linear size $L = 128\Delta l$ ($\Delta l = 1.0$) with a dimensionless time step of 0.001. The boundary conditions are periodic. Initial conditions are determined according to the specific modelling task (see below).

3. Results of Modelling

This section discusses the results of numerical simulations. It begins with the results of modelling the precipitation of β-phase precipitates in the ternary alloy Zr–1%Nb–1%Sn without irradiation. Next, it explores the precipitation of precipitates in the binary alloy Zr–2%Nb with annealing and neutron irradiation, taking into account the dynamics of point defects with their sinks. The formation of precipitates during irradiation in the ternary alloys Zr–2%Nb–0.5%Sn and Zr–0.4%Nb–0.5%Sn is also investigated.

3.1. Precipitation of β-Phase in Zr–1%Nb–1%Sn during Annealing

This subsection is dedicated to the investigation of the dynamics, statistical properties, and mechanical properties of β-phase precipitates and dislocation loops in the ternary alloy Zr–1%Nb–1%Sn. Subsection 3.1.1 presents the results of modelling precipitation with a statistical analysis. The results of the study of mechanical properties are presented in subsections 3.1.2 and 3.1.3. The strengthening of the alloy due to β-phase precipitates is explored, including the modelling of external mechanical loading in the form of shear deformation and compression. The yield and tensile strength limits are determined at different shear rates, and an analysis of the interaction between dislocation loops and precipitates is performed.

3.1.1. Dynamics of β-Phase Precipitation

The dynamics of the system during annealing are described by Eqs. (8). Initially, niobium and tin impurities are homogeneously dissolved in the zirconium matrix with nominal concentrations: niobium $\bar{c}_{\mathrm{Nb}} = \bar{c}_{\mathrm{Sn}} = 0.01$:

$\langle c_{\mathrm{Nb}}(\mathbf{r}, t = 0)\rangle = \overline{c}_{\mathrm{Nb}}$, tin $\langle c_{\mathrm{Sn}}(\mathbf{r}, t = 0)\rangle = \overline{c}_{\mathrm{Sn}}$, and zirconium $\langle c_{v}(\mathbf{r}, t = 0)\rangle = c_{v0}$, $\langle(\delta c_{\mathrm{Nb}}(\mathbf{r}, t = 0))^2\rangle = 0.01\overline{c}_{\mathrm{Nb}}$, $\langle(\delta c_{\mathrm{Sn}}(\mathbf{r}, t = 0))^2\rangle = 0.01\overline{c}_{\mathrm{Sn}}$, $\langle(\delta c_{v}(\mathbf{r}, t = 0))^2\rangle = 0.01 c_{v0}$; c_{v0} represents the equilibrium concentration of vacancies. The concentration of zirconium is calculated using the law of mass conservation.

During the heat treatment, β-Nb precipitates are formed in the solid solution. In Figure 1 (panel *a* and *b*), taken at real-time moments t = 54 hours and 90 hours, we observe the presence of β-Nb precipitates. In Figure 1, we can see that tin is mostly uniformly distributed in the volume with slight local deviations from a homogeneous state around the precipitates, where c_{Sn} is slightly higher than in the α-matrix. This effect is caused by the attractive interaction between tin atoms and vacancies, which is well depicted by the local distribution of equilibrium vacancies shown in Fig. 1, panel *c*. The vacancy concentration at the interphase boundaries exceeds the equilibrium value, and tin atoms are predominantly localized near these domains.

Quantitative investigation of precipitate formation can be conducted by examining the dynamics of dispersions $\langle(\delta c_{\mathrm{Nb}})^2\rangle$ and $\langle(\delta c_{\mathrm{Sn}})^2\rangle$, as shown in Fig. 2, panel *a*, where the dispersion plays a role as an effective order parameter for precipitate formation, analogous to structural ordering phenomena [105]. An increase in dispersion indicates the formation of dense and diluted domains of the respective component within the volume. In the real system, the growth of niobium concentration dispersion is associated with the formation and growth of β-Nb precipitates in the α-matrix. The increase in tin concentration dispersion corresponds to tin segregation in domains enriched with vacancies (tin-captured) surrounding the β-Nb precipitates.

The profiles shown in Fig. 2, panel *b*, illustrate the distribution of tin and vacancy concentrations near the precipitate. It is evident that elevated tin concentration values are located in vacancy-enriched regions outside the precipitates. The vacancy concentration inside the precipitates is lower than in the matrix phase due to higher vacancy formation energy in the β-Nb phase compared to the α-Zr phase. Additionally, the tin content within the precipitates is exceptionally low compared to the matrix phase (see Table 1).

For the purpose of performing a statistical analysis of precipitate kinetics, let us consider the evolution of the number density of precipitates, N_p, and their average radius of spherical precipitates, $\langle R_p\rangle$, as shown in Fig. 3, panel *a*. In the computational procedure, we count all precipitates containing $c_{\mathrm{Nb}} \geq c_{\mathrm{Nb}}{}^{\beta}$, where $c_{\mathrm{Nb}}{}^{\beta} = 0.63$, which is the threshold used for niobium concentration in the β-Nb phase. Consequently, the average size and number density of precipitates increase to their respective fixed values. On these time scales, there is no observable coales-

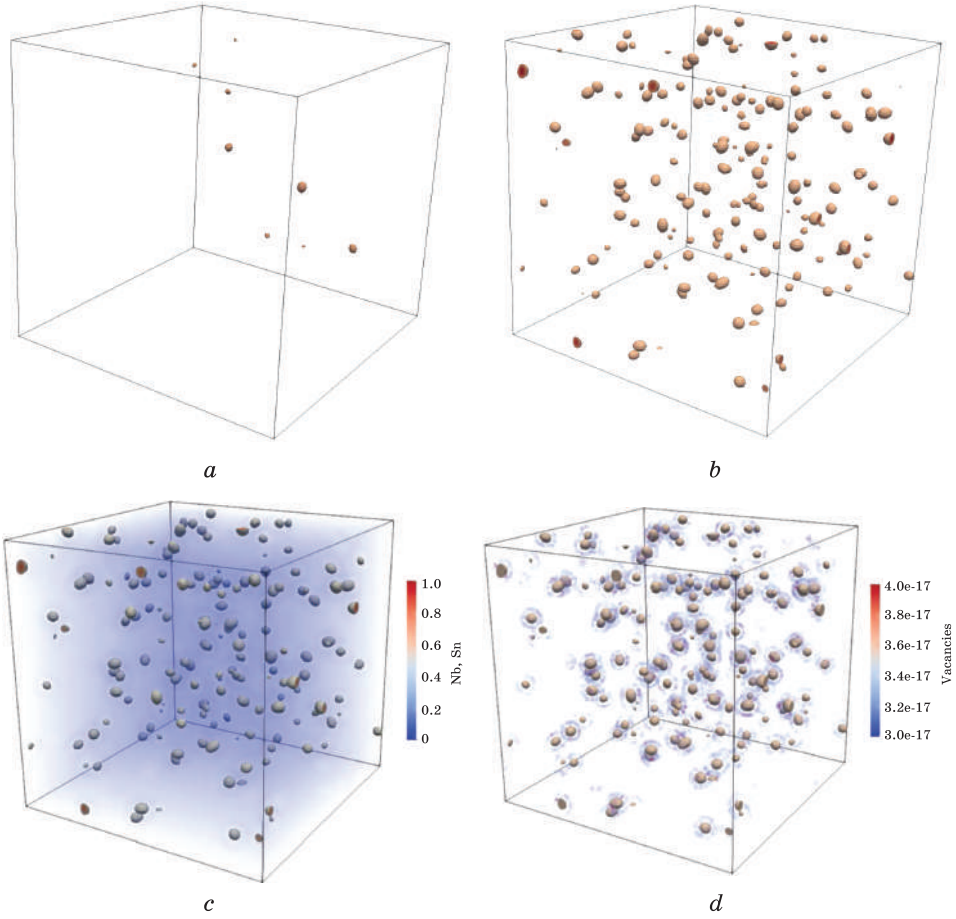

Fig. 1. Precipitates evolution at thermal treatment of the solid solution at 550 K. Snapshots illustrating precipitates of β-phase at t' ρ 460 (*a*) (nuclei of β-phase precipitates with Nb content >10% inside) and $t' = 1000$ (*b*) (Nb content is >60%). Snapshots of spatial rearrangement of tin (*c*) and vacancies (*d*) around precipitates [76]

cence regime. The calculated distance $L = (2\langle D_p \rangle N_p)^{-1/2}$ [106] with between precipitates of size $\langle D_p \rangle = 2\langle R_p \rangle$ is about 100 nm. The obtained values of precipitate size, their number density, and the average distance between precipitates align well with experimental observations and modelling results [7–14].

The dynamics of the volume fraction of precipitates, V_f, is presented in Fig. 3, panel *b*. Here, we observe an increase in V_f during precipitate formation, which is in good agreement with the results and the predicted scenario described in a study [107] after annealing for 500 hours. The slow dynamics of V_f and the corresponding growth in the average precipitate radius and number density (see Fig. 3, *a*) are associated not

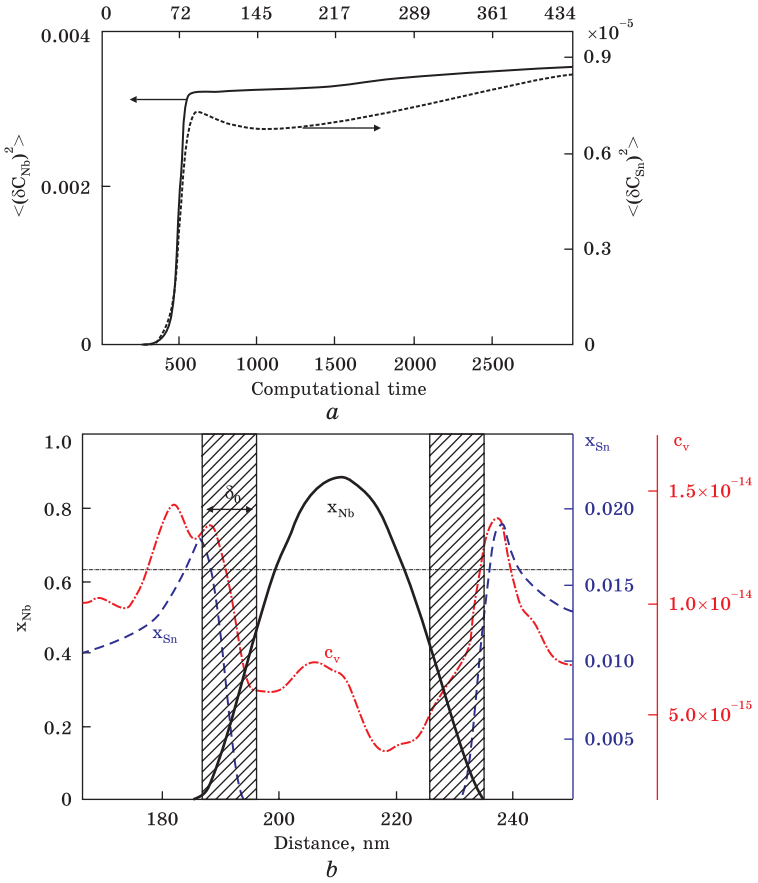

Fig. 2. Protocols of dispersion of Nb and Sn concentrations (*a*). Typical profiles of Nb, Sn and vacancy concentrations around β-precipitate (*b*) [76]

only with the low niobium content but also with the trapping of vacancies by tin, which hinders niobium diffusion within the bulk towards the precipitates.

As shown in Figure 3, the dependence reveals that the niobium content in precipitates reaches a constant value of approximately 80%, while the Nb content in the matrix $c^m_{Nb} = (\overline{c}_{Nb} - V_f c^{\beta}_{Nb})/(1 - V_f)$ decreases over annealing time. In Figure 3, panel *d*, we observe that the statistical size distribution of precipitates is close to the Lifshitz–Slyozov–Wagner distribution (panel *c*) [108, 109].

3.1.2. Hardening by Precipitates

As known, the material strengthening is described as the square root of the sum of the squares of strengthening components, primarily associated with the dislocation network, grain boundaries, matrix-dissolved

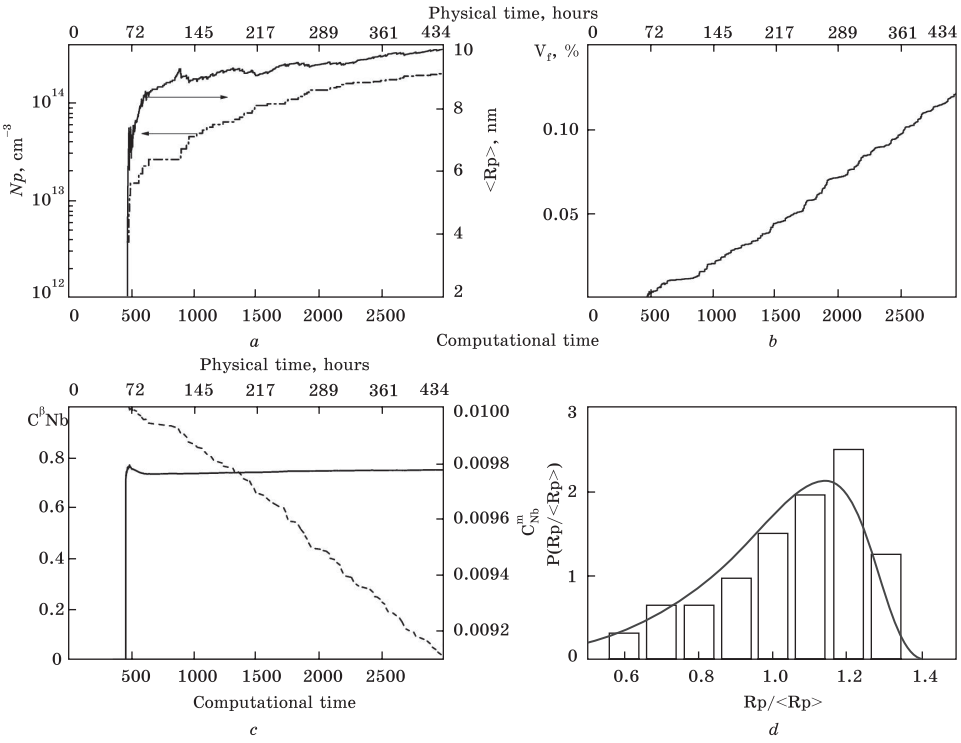

Fig. 3. Dynamics of precipitates number density and their mean size (*a*). Volume fraction of precipitates (*b*). Protocols of the content of Nb in precipitates $c_{\mathrm{Nb}}\beta$ and in the matrix $c_{\mathrm{Nb}}m$ (*c*). Distribution of precipitates over size (histogram illustrates calculated data; solid line relates to classical Lifshitz–Slyozov–Wagner distribution) (*d*) [76]

elements, precipitates, and other structural defects that impede dislocation motion [110]. The microstructure of the material continuously changes during thermal treatment, resulting in alterations in the overall strength of the material. In this work, we focus on the strengthening of the material due to β-phase precipitates. The materials' strength is proportional to the density and size of these precipitates. To calculate the corresponding increase in the yield strength, $\Delta\sigma_y^{\beta}$, required to detach dislocations from precipitates, we use the formalism developed in Ref. [111] and its generalization for randomly distributed precipitates [112]. Thus, the increase in yield strength is estimated by the formula [112]:

$$\Delta\sigma_y^{\beta} = \frac{1}{2\pi}\frac{\mu_0 b}{L-\langle D_p\rangle}\frac{1}{\sqrt{\ln(L/r_c)}}\left[\ln\left(\frac{\langle\bar{D}_p\rangle}{r_c}\right)+0.7\right]^{3/2}. \qquad (19)$$

Here, the shear modulus μ_0 is defined by the corresponding bulk modulus $K_0 = V_f K_{\mathrm{Nb}} + (1 - V_f)K_{\mathrm{Zr}} + \bar{c}_{\mathrm{Sn}} K_{\mathrm{Sn}}$ as $\mu_0 = 3K_0(1 - 2\upsilon)/2(1 + \upsilon)$,

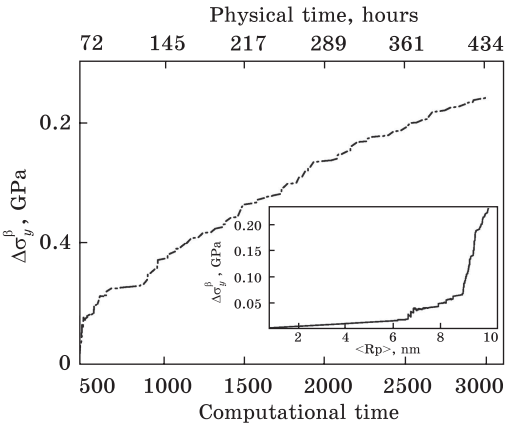

Fig. 4. Precipitate yield strength dynamics and its dependence on the precipitate radius (see inset) [76]

$\langle \bar{D}_p \rangle = \langle D_p \rangle L/(\langle D_p \rangle + L)$ is harmonic average, $r_c = 3b$ is the dislocation core radius.

The time evolution of the yield strength increment $\Delta\sigma_y{}^\beta$, as obtained from the size and number density of precipitates, is illustrated in Fig. 4. It is evident that the contribution to the yield strength from precipitates increases with the annealing time and with the increase in precipitate size $\langle R_p \rangle$ (see the insert in Fig. 4). The corresponding contribution to strengthening from precipitates reaches up to 250 MPa for precipitate sizes of approximately 20 nm. This obtained value of strengthening is in close agreement with the results discussed in an experimental study [113].

3.1.3. Modelling Mechanical Loads

In order to study the mechanical response of the system to external loads, we employ a theoretical framework based on the approaches developed in the works [58, 114–118]. We introduce the elastic displacement field u and the strain tensor in the standard way: $\varepsilon_{ij} \equiv (\partial_i u_j + \partial_j u_i)/2$ with $i, j \in \{x, y, z\}$. Neglecting the contribution of the equilibrium vacancy concentration due to its minor impact on the mechanical properties of the studied system, the elastic energy of the system can be expressed as:

$$G_{el}(u, \{c_\mu\}) = \frac{K}{2} e_{ii}^2 + \Phi(\{e_{i,j}\}) + G_{el}^c(e_{ii}, \{c_\mu\}) . \qquad (20)$$

Here, we are considering a more general case where the bulk modulus of elasticity K depends on concentration $K = K(\{c_\mu\})$. The second term on the right-hand side of Eq. (20) describes the elastic contributions responsible for volumetric and shear deformations, taking into account the crystallographic symmetry of the system. The third term accounts for the feedback between composition and dilatational strain ε_{ii}.
For the bulk modulus, here, we put [119]

$$K = K_0 + K_1 \Delta c_{\mathrm{Nb}}, \quad K_1 = \frac{K_{\mathrm{Nb}} - K_{\mathrm{Zr}}}{c_{\mathrm{Nb}}^\beta - c_{\mathrm{Nb}}^m}, \quad \Delta c_{\mathrm{Nb}} = c_{\mathrm{Nb}} - c_{\mathrm{Nb}}^m . \qquad (21)$$

For elastic contribution $\Phi(\{\varepsilon_{ij}\})$, we exploit the relation

$$\Phi(\{\varepsilon_{ij}\}) = \Theta(e_2, e_3) + \Psi(e_4, e_5, e_6) , \qquad (22)$$

where the contribution of uniaxial elastic energy $\Theta(e_2,e_3)$, which characterizes the change in elastic energy due to compressive or tensile deformation, takes the form:

$$\Theta(e_2,e_3)=\frac{\mu}{8\pi^2}\left[3-\cos(2\pi e_+)-\cos(2\pi e_-)-\cos\left(\frac{4\pi e_3}{\sqrt{3}}\right)\right], \qquad (23)$$

for the contribution of shear elastic energy, we have:

$$\Psi(e_4,e_5,e_6)=\frac{\mu}{4\pi^2}\left[3-\cos(2\pi e_4)-\cos(2\pi e_5)-\cos\left(2\pi e_6\right)\right]. \qquad (24)$$

The shear modulus μ is conventionally related to the bulk modulus K as follows. To determine the elementary components of deformation, we use:

$$\begin{gathered} e_1=\partial_x u_x+\partial_y u_y+\partial_z u_z, \quad e_2=\partial_x u_x-\partial_y u_y, \\ e_3=(2\partial_z u_z-\partial_x u_x-\partial_y u_y)/\sqrt{3}, \quad e_4=\partial_x u_y+\partial_y u_x, \\ e_5=\partial_y u_z+\partial_z u_y, \quad e_6=\partial_z u_x+\partial_x u_z. \end{gathered} \qquad (25)$$

The deformations e_2 and e_3 are tetragonal ones, e_4, e_5 and e_6 are shear deformations, where $e_\pm \equiv e_2 \pm e_3/\sqrt{3}$. For small deformations in linear elasticity theory, we obtain the standard constructs $\Theta \cong \mu({e_2}^2 + + {e_3}^2)/2$ and $\psi \cong \mu({e_4}^2 + {e_5}^2 + {e_6}^2)/2$. Additional elastic contribution ${G_{el}}^c$, caused by lattice mismatch according to Vegard's law, is taken in the form [58, 114–118]

$$G_{el}^c=\alpha e_1 \Delta c_{\mathrm{Nb}}. \qquad (26)$$

For the coupling parameter $\alpha > 0$, which characterizes the compositional response and volume change, we set $\alpha = 2\mu_{\mathrm{Nb}}$.

The dynamics of the elastic displacement vector $\mathbf{u}$ under mechanical loads is described by the following equation [58]

$$\rho\frac{\partial \mathbf{v}}{\partial t}=\eta_0\nabla^2\mathbf{v}+\nabla\cdot\ddot{\sigma}, \qquad (27)$$

where $\mathbf{v}=\partial\mathbf{u}/\partial t$ is the lattice speed, ρ is the mass density, η_0 plays a role of shear viscosity, $\ddot{\sigma}=\{\sigma_{ij}\}$ is symmetrical stress tensor with diagonal, $\sigma_{ii}=\partial G_{el}/\partial\varepsilon_{ii}$, and non-diagonal, $\sigma_{ij}=(1/2)\partial G_{el}/\partial\varepsilon_{ij}$, $i\neq j$, components.

We apply external mechanical loads in the form of shear deformation $\gamma=\dot{\gamma}t$ and uniaxial compression deformation $\varepsilon=\dot{\varepsilon}t$ with a constant strain rate $\dot{\gamma}$ and $\dot{\varepsilon}$, respectively. Then, we numerically solve Eq. (27), using an annealed microstructure as the initial configuration for the elastic fields specified as $\mathbf{u}=0$ and $\mathbf{v}=0$.

We impose boundary conditions for the elastic displacement vector $\mathbf{u}$ as follows: for shear deformation $u_x=\gamma z$, $u_y=0$, $u_z=0$; for compression, $u_x=1/2\varepsilon z$, $u_y=1/2\varepsilon z$, $u_z=-\varepsilon z$. Referring to works [112, 120–123], we conduct simulations with strain rates ranging from 5×10^7 s^{-1} up to

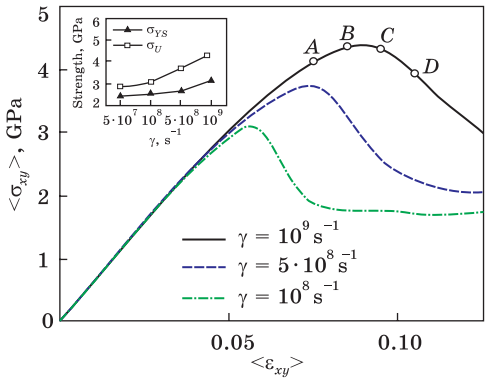

Fig. 5. Strain–stress curves at different strain rates. Inset shows dependences of ultimate stress and yield stress on shear rate. Markers *A*, *B*, *C*, and *D* correspond to deformations $\langle\varepsilon_{xy}\rangle$ = 0.075, 0.085, 0.095, 0.105 [76]

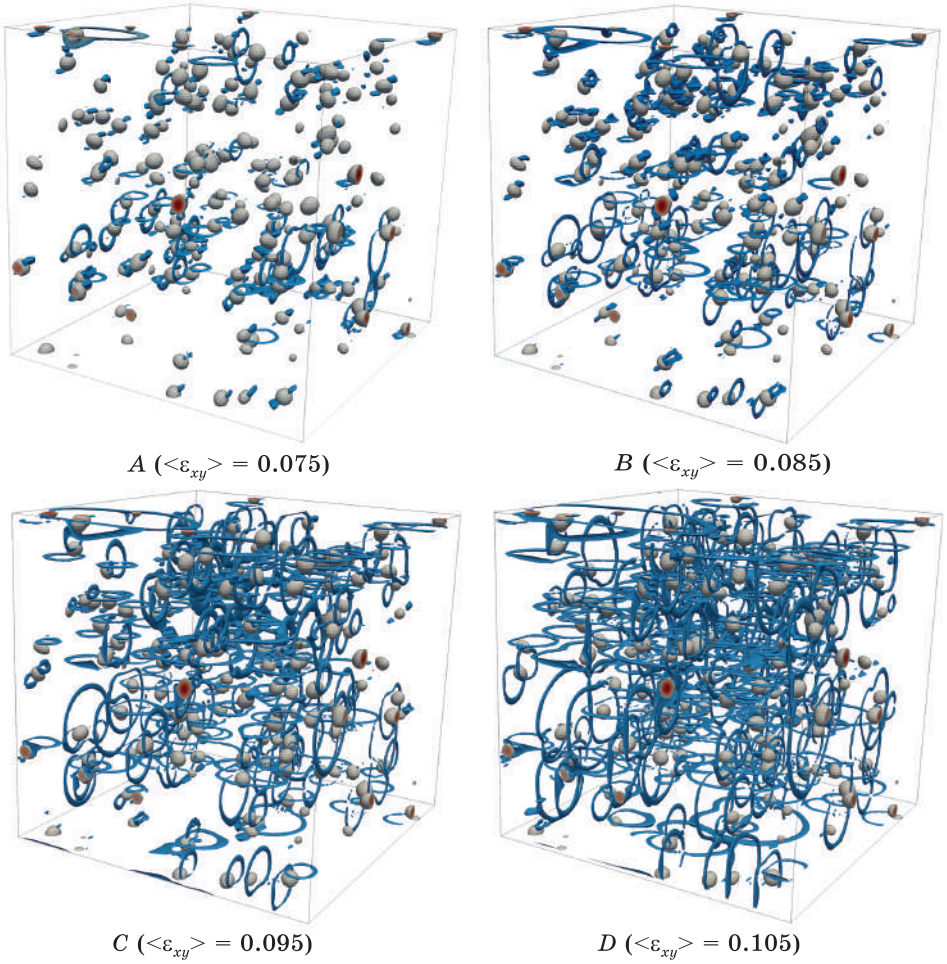

Fig. 6. Evolution of dislocation loops at shear deformation (snapshots correspond to deformations at points *A*, *B*, *C*, and *D* shown in the previous figure) [76]

10^9 s^{-1}. As well known, with increasing strain rate, there is a significant increase in the yield strength and ultimate strength.

In Figure 5, deformation curves for shear deformation of the investigated Zr–1%Nb–1%Sn alloy are shown at different strain rates, $\dot{\gamma}$. The transition from elastic deformation to plastic deformation corresponds to the yield point, σ_{YS}, which characterizes the material's resistance to plastic deformation. The ultimate strength, σ_U, corresponds to the maximum stress values on the stress–strain diagram that the material can withstand before failure. It is evident that an increase in the strain rate leads to an increase in both yield strength and ultimate strength. Furthermore, with an increased strain rate, the ultimate strength is reached at a later point (at a higher strain). The dependence of yield strength and ultimate strength on the shear strain rate is shown in the insert in Fig. 5. The corresponding increasing dependences with increasing shear strain rate are well matched to the standard deformation scenario at various shear rates. These increasing dependences are explained by the increase in dislocation (loop) density with increasing strain rate [124]. The decrease in deformation curves and dislocation loop density signifies a reconstruction of the slip planes by forming percolation clusters due to the interaction of dislocation loops, promoting the transition to plastic flow.

To monitor the development of the dislocation structure, we study the distribution of elastic fields, allowing us to observe the evolution of slip planes within the specimen by examining the evolution of dislocation loops. Slip planes correspond to the maximum shear strain values e_4. It is evident that an increase in external deformation leads to an increase in the number and size of slip planes. The edge of a slip plane corresponds to a dislocation loop formed during deformation. In these edge points, local values of the elastic energy density ψ are maximal. In Figure 6, where loops correspond to the maximum ψ values, we can see that the orientations of the slip planes under shear loading correspond to the most favourable slip directions, in line with the results of the work [114]. The observed dislocation structure develops from slip planes (in the form of small clusters). With increased deformation, dislocation loops form (see the snapshot at $\langle \varepsilon_{xy} \rangle = 0.075$ in Fig. 6, corresponding to point *A* in Fig. 5). Loop glide primarily occurs in the softer phase.

Initially, dislocation loops form around β-Nb precipitates in the region between phase boundaries, which is in good agreement with results obtained in other studies [116, 118]. Increased external deformation leads to an increase in the number and size of dislocation loops in the softer phase of the sample, characterized by a lower elastic modulus compared to the harder regions corresponding to precipitates with higher elastic modulus values. Niobium precipitates primarily hinder loop glide in one direction (snapshot at $\langle \varepsilon_{xy} \rangle = 0.085$ in Figure 6, corresponding to

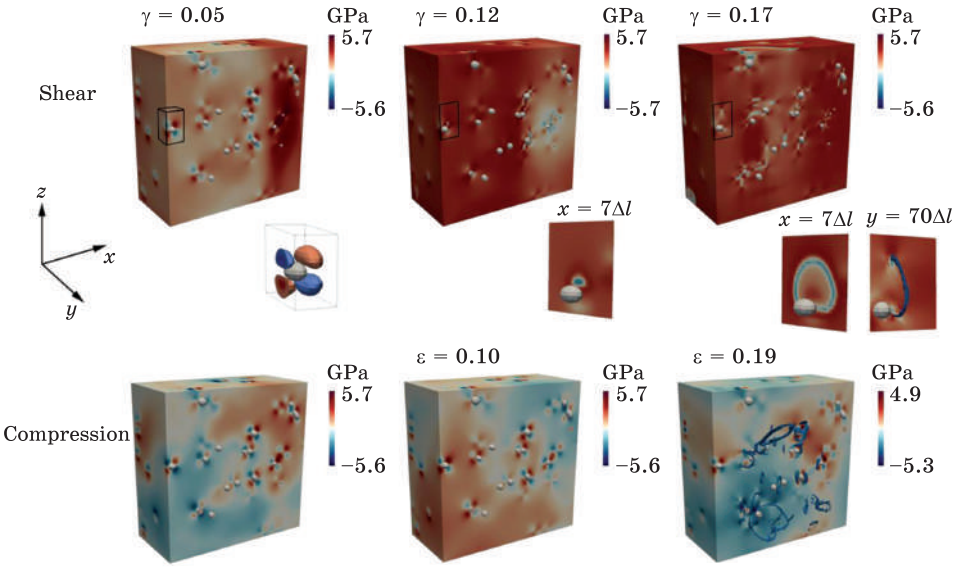

Fig. 7. Shear stress σ_{xy} evolution under shear and compressive strain

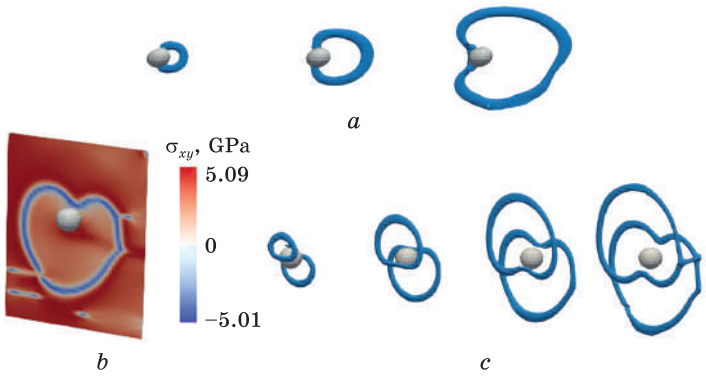

Fig. 8. Growth of dislocation loops around precipitate: dynamics of the single loop (*a*); a map of local shear stress values around precipitate and loops (*b*); evolution and interaction of two loops (*c*) [76]

point *B* in Fig. 5). Here, slip planes tend to intersect each other, resulting in the formation of complex dislocation curves and clusters. With further increased deformation, $\langle\sigma_{xy}\rangle < \sigma_U$, which is associated with dislocation loop interactions and the development of an extended dislocation structure (snapshot $\langle\varepsilon_{xy}\rangle = 0.095$ in Fig. 6, corresponding to point *C* in Fig. 5). At higher deformations, far from the yield strength limit, a percolation structure forms, corresponding to the final stage of the plastic deformation process before failure (snapshot at $\langle\varepsilon_{xy}\rangle = 0.105$ in Fig. 6, corresponding to point *D* in Fig. 5).

Next, let us examine the evolution of elastic stresses in the investigated Zr–1%Nb–1%Sn alloy sample under shear deformation (γ) and compression (ε) loading. In Figure 7, snapshots of the distributions of

shear stresses (σ_{xy}) are presented together with β-Nb precipitates. Additionally, the inserts show local stress redistributions near precipitates with subsequent dislocation loop formation. As we can observe, at initial deformations (snapshots at shear deformation $\gamma = 0.05$ and compression deformation $\varepsilon = 0.05, 0.1$), stresses in the sample are distributed in such a way that the maximum absolute values of σ_{xy} are concentrated around the precipitates. With further increasing deformation, within the areas influenced by maximum shear stresses σ_{xy}, once they reach a critical value (the critical resolved shear stress) in one of the slip systems, according to Schmid's law [125], the formation of slip planes begins, and dislocation loops nucleate. In other words, a transition to plastic deformation of the material occurs. At this stage, within the formed slip plane, due to increasing internal deformations, a region of negative stresses σ_{xy} emerges, as shown in the inset to the snapshot at a shear deformation of $\gamma = 0.12$ (Fig. 7). Furthermore, as the size of the slip planes increases and dislocation loops grow, the maximum in absolute value of the shear stresses σ_{xy} concentrates in the vicinity of the dislocation core. Specifically on opposite sides of it (see insets in the snapshot at a shear deformation of $\gamma = 0.17$ in the slip plane $x = 7\Delta l$ and perpendicular to it in the plane $y = 70\Delta l$). The dislocation structure formed during compression is shown in the last snapshot of shear stresses at $\varepsilon = 0.19$ (Fig. 7). It should be noted that in the investigated plastic deformation in the form of shear and compression, the slip occurs along crystallographic planes with the most favourable orientation relative to the applied load, characterized by Schmid's orientation factor [114, 116, 118, 125].

Next, let us discuss the growth of dislocation loops near the β-Nb precipitates and the interaction of the 'dislocation loop–precipitate', as presented in Fig. 8. As we can see, the precipitate captures a segment of the loop, causing its growth to be restrained (see images in Fig. 8, *a*). This behaviour is well correlated with the Orowan's mechanism, which is described by the difference in elastic moduli between the precipitate phase and the matrix phase. Loops are predominantly emerged around interphase regions, and loop segments localized near precipitates remain anchored. Segments of the loop outside the precipitate grow in a more elastically soft region characterized by a lower modulus of elasticity. According to the Orowan's mechanism, as stresses increase, mobile dislocations bypass the obstacle and leave a loop behind. The loop left behind increases the effective size of the obstacle. Therefore, the process of loop formation leads to material strengthening due to deformation. This effect can also be explained by the interaction of loops with precipitates through elastic fields that occur during deformation (see Fig. 8, *b*). It is evident that the shear stresses σ_{xy} in terms of modulus are lower inside the slip plane bounded by the curve corresponding to

the dislocation loop compared to their values outside the loop. Consequently, loops will grow to compensate for the emerging difference in shear stresses. Thus, the mismatch in elastic moduli leads to slip outside the precipitates being more favourable, while the additional stresses induced by the precipitates resist slipping. A typical interaction of loops is shown in Fig. 8, *c*. Here, we can observe the formation of additional segments due to the reduction in accumulated stress around the loops. As a result, two or more loops may merge into one, reducing the overall loop density and forming percolation clusters. Due to the observed interaction of dislocations with precipitates, causing the accumulation of dislocation loops at the matrix–precipitate interphase boundaries, a robust network (dislocation structure) is formed, resulting in a significant deformation strengthening effect [126, 127]. As we can see, dislocations can slip through precipitates and bypass them according to the Orowan's bypass mechanism depending on external stresses. A similar effect of dislocation pinning by hard β-Nb precipitates in Zr–Nb alloys, based on the Orowan's mechanism, was observed in experiments (see, for example, [113]).

3.2. Precipitate Formation in Irradiated Zr–2%Nb Alloy

In this section, we model the formation of precipitates in the binary Zr–2% Nb alloy through thermal treatment and neutron irradiation. Two stages are discussed separately: annealing of the alloy at 550 K (see section 3.2.1), starting from a random configuration, and radiation-induced precipitate formation under various reactor conditions (see section 3.2.2). Here, our focus is on the kinetics of precipitation from the recombination of point defects and the stability of precipitates under irradiation. In section 3.2.3, a general assessment of strengthening is conducted, and the increase in yield strength due to radiation-induced precipitates is calculated.

3.2.1. Evolution of the β-Phase during Annealing

Considering that all niobium is in the β-phase, we associate the process of β-phase precipitate formation with the creation of niobium-enriched domains during phase separation, starting from an initially homogeneous solution. We examine a binary alloy with 2% niobium content as a model system for Zr–Nb alloys. Initially, for the thermal treatment procedure, we set random values for Nb content: $\langle c_{\mathrm{Nb}}(\mathbf{r}, t = 0)\rangle = 1 - \bar{c}$, $\langle c_v(\mathbf{r}, t = 0)\rangle = c_{v0}$, $\langle (\delta c_{\mathrm{Nb}}(\mathbf{r}, t = 0))^2\rangle = 0.01(1 - \bar{c})$, $\langle (\delta c_v(\mathbf{r}, t = 0))^2\rangle = 0.01 c_{v0}$. Subsequently, we calculate the concentration of zirconium according to the mass conservation law and simultaneously solve Eqs. (13) and (14) with the law of mass conservation, employing expression (11) for the thermodynamic flux. Here, we investigate the statistical properties of

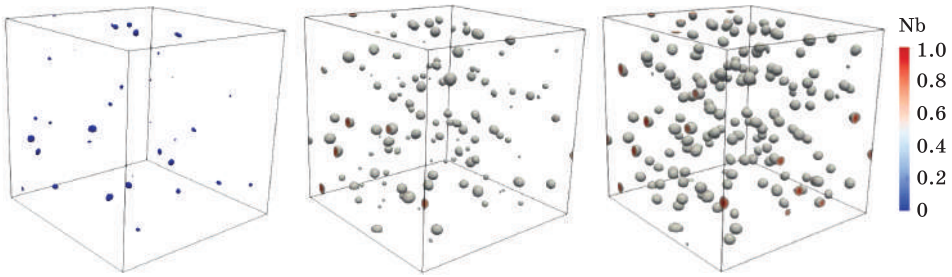

Fig. 9. Typical snapshots of Nb precipitation during the thermal treatment at dimensionless time instants 600, 800, 1200 (from left to right) at 550 K [75]

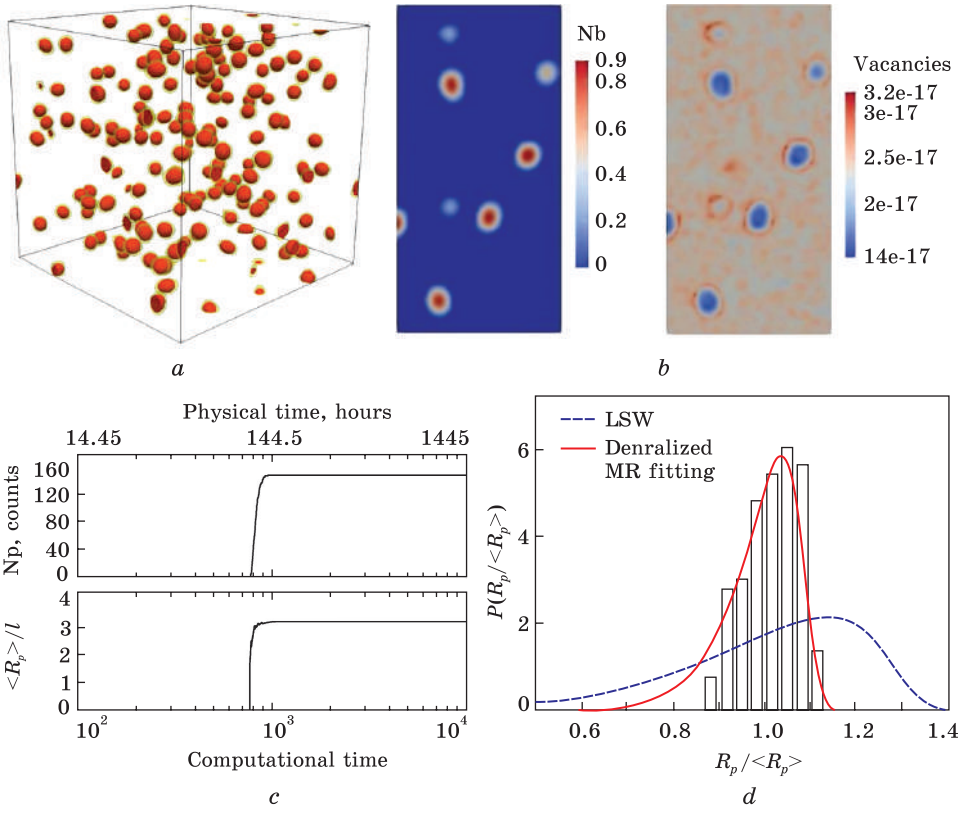

Fig. 10. Precipitates formed at aging of the alloy at 550 K. Snapshot of precipitates of β-phase (*a*). Snapshots of Nb and vacancy concentrations in the quasi-stationary regime (*b*). Dynamics of the number of precipitates and mean radius of precipitates $\langle R_p \rangle$ measured in units l (*c*). Distribution function over precipitate size in quasi-stationary regime: dashed curve relates to Lifshitz–Slyozov–Wagner distribution, solid curve corresponds to generalized Marqusee and Ross distribution (*d*) [75]

β-phase formation during thermal treatment, considering only equilibrium vacancies.

Figure 9 illustrates snapshots of the evolution of the system with the formation of the β-Nb phase in the α-Zr matrix. It is evident that with increasing annealing time, both the number and average size of precipitates grow. The microstructure of the alloy annealed at $T = 550$ K is shown in Fig. 10, *a*. In this microstructure, β-phase precipitates (shown in red) are covered with vacancies with a concentration exceeding the equilibrium value (the corresponding vacancy concentration is depicted in yellow). According to the concentration fields of niobium and vacancies, as displayed in Fig. 10, *b*, we can conclude that most of the vacancies with concentrations above equilibrium are located at the phase boundaries. This is consistent with the results from positron annihilation spectroscopy [7]. Such a distribution of vacancy concentration is associated with different types of interactions between niobium and zirconium atoms with vacancies in the thermodynamic potential. Hence, the vacancy concentration in the β-phase is lower than the equilibrium value. The concentrations of vacancies and niobium in the α-phase are distributed almost uniformly. Most of the precipitates have a spherical shape with small anisotropy.

The dynamics of the number of precipitates (Np) and their average radius, $\langle R_p \rangle$, are presented in Fig. 10, *c*. The calculated quantity of precipitates increases rapidly after a certain transition time (physical time approximately 50 hours), transitioning to a quasi-steady-state regime. In this regime, only small local disturbances in concentration may occur within the matrix as the system relaxes towards thermodynamic equilibrium. The transition time for the emergence of well-defined precipitates aligns well with the experimentally observed time scale [128]. To find the average radius of the precipitates, we compute the volume of all precipitates and then divide it by the number of precipitates. In the quasi-steady-state regime, the average size of precipitates that contain at least 70% niobium is $\langle R_p \rangle / l \approx 3$. The average distance between precipitates of average size, uniformly distributed in a volume of L^3, is approximately $\approx 24l$, a value that can be easily calculated considering the properties of a densely packed lattice. This leads to an estimated average size of precipitates of $2R_p \approx 30$ nm and an average distance between them of ≈100 nm. The calculated number density of precipitates after annealing is approximately 5.7×10^{14} cm^{-3}. For the volume fraction of precipitates ($n_p \approx N_p(4\pi\langle R_p \rangle^3/3L^3)$)), we obtain $n_p \approx 0.01$–0.02. The obtained values for the average precipitate size, the density of precipitates, the distance between precipitates, and the volume fraction are in good agreement with many experimental results. For instance, experimental data on niobium precipitate statistics show values of precipitate diameter in the range of 13–57 nm with densities of $(1–4) \times 10^{14}$ cm^{-1}

at temperatures ranging from 573–873 K [7–13]. In a separate study of the Zr–Nb–Fe alloy, 20 nm niobium precipitates were observed [129]. Experimental investigations on Zr–2.5% Nb–0.5% Cr showed that in the non-irradiated system, β-phase precipitates had a size of ≈13 nm at 576 K [14].

The statistical analysis of the precipitate size distribution function, $P(R_p/\langle R_p\rangle)$, exhibits the form of the Lifshitz–Slyozov–Wagner distribution with tails observed for $R_p < \langle R_p\rangle$ (see Fig. 10, *d*). It should be noted that the original Lifshitz–Slyozov–Wagner distribution [108, 109] is not a direct fit because it has an extended spectrum of particles by size (as shown by the dashed curve in Fig. 10, *d*). A more accurate approximation (as shown by the solid curve) is obtained using the Marqusee and Ross approach. This is associated with the slow dynamics of $\langle R_p\rangle$, which is governed by the diffusion coefficient $D(R_p)$ μ $1/R_p^4$ for precipitates in binary alloys, dependent on precipitate size (details can be found in Ref. [130]). Here, we assume that nucleation or coalescence of particles during their coarsening process does not occur.

3.2.2. Radiation-Induced Precipitation

In this subsection, we investigate changes in the statistical properties of the microstructure under neutron irradiation under different conditions. We also consider the alteration of mechanical properties under the influence of irradiation. To study the stability of the initial microstructure and radiation-induced precipitation of precipitates, we utilize a previously prepared (annealed) system with the microstructure shown in Fig. 10 as the target (initial conditions for modelling). We simulate neutron irradiation at different temperatures and dose accumulation rates, corresponding to reactor conditions. We consider the case where defect sinks are distributed throughout the system, and simultaneously solve Eqs. (13)–(18).

The typical scenario of new precipitate formation in the system with the annealed microstructure under prolonged irradiation is depicted in Fig. 11. The precipitates formed during annealing are represented by domains in red, while the blue domains illustrate precipitates induced by irradiation. New precipitates are shown here with sizes exceeding the lattice constant *l* and containing a niobium concentration of over 70%. As the irradiation dose accumulates, both the number and size of precipitates increase (compare images at different doses in Fig. 11, *a*, *b*). Figures 11, *c* and *d* illustrate the concentration of out-of-equilibrium vacancies surrounding the precipitates. The concentration of these vacancies exceeds their equilibrium value by several orders of magnitude; so, only high values of vacancy concentration located at the interfacial boundaries are shown for all precipitates in the system, as seen in unirradiated samples. The concentration of vacancies within β-precipitates

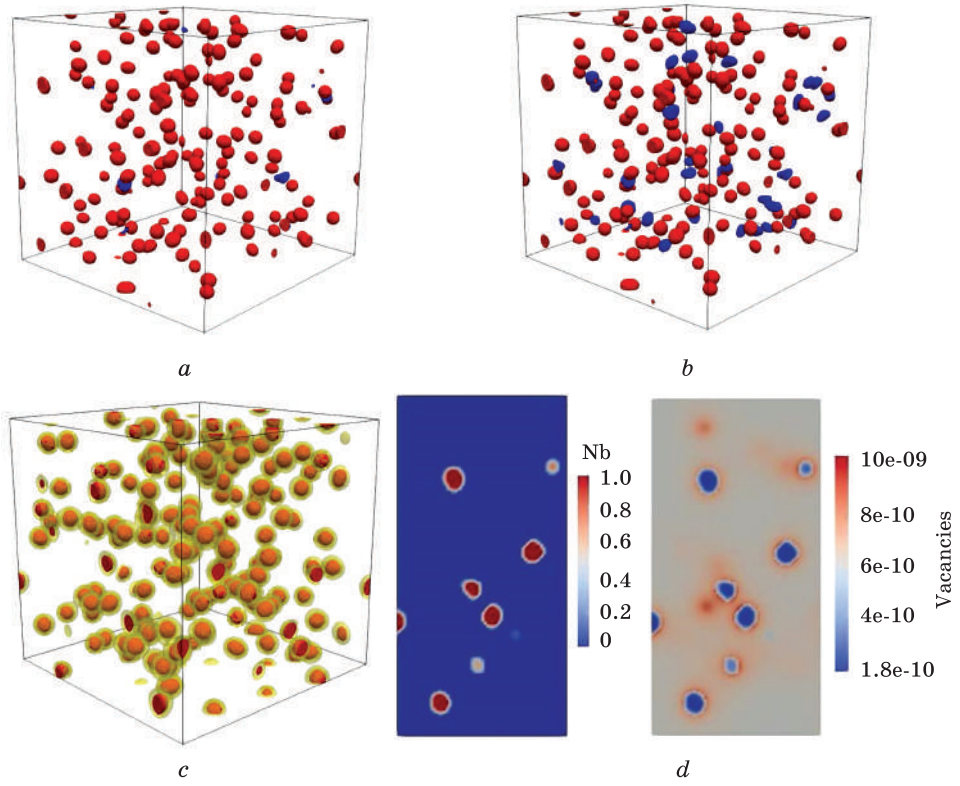

Fig. 11. Precipitation under irradiation at 550 K and $K = 10^{-6}$ dpa/s. Snapshots are shown at different doses: 1 dpa (*a*), 2 dpa (*b*). Microstructure of the irradiated alloy with vacancy field at 1 dpa (*c*). Two-dimensional snapshots of Nb and vacancy concentration fields at 2 dpa (*d*) [75]

is extremely low compared to their values within the α-matrix (see Fig. 11, *d*). This process demonstrates the radiation-induced formation of precipitates and their effect on the local vacancy concentration, which can significantly alter the material's properties.

Next, let us examine the dose dependences of the total number of precipitates, N_p, and the average precipitate radius, $\langle R_p \rangle$, under various irradiation conditions, as shown in Fig. 12. Initially, it is worth noting that the quantity of precipitates remains constant, while the average radius of the precipitates decreases at small doses. This reduction is due to the dissolution of existing precipitates, caused by the creation of a large number of vacancies at low doses, leading to a local reduction in β-Nb particles due to the blurring of interfacial boundaries. This situation is typical of radiation-induced dissolution of precipitates, as observed in previous works [47, 51, 131]. This aligns well with the findings of the study [131], which showed that in the presence of an excess

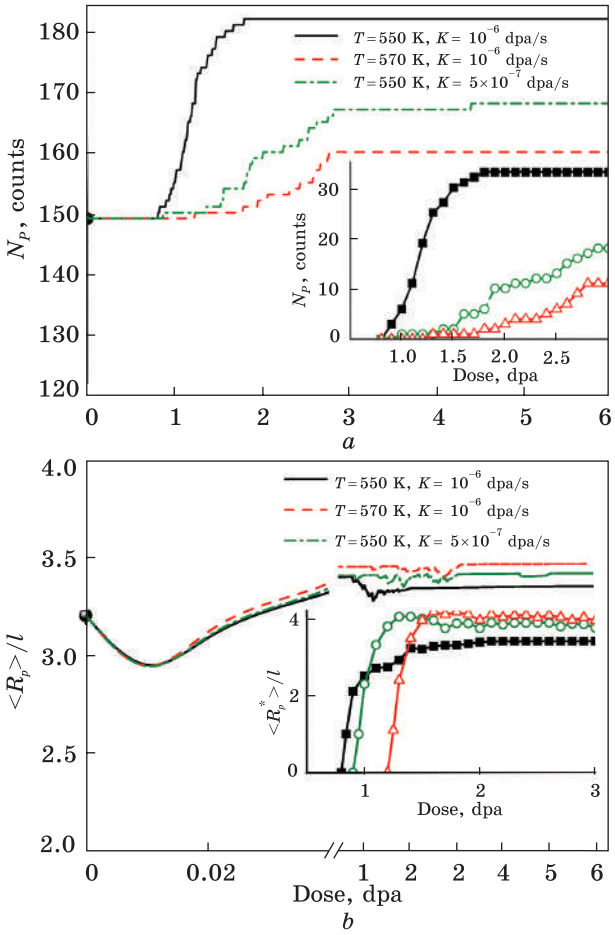

Fig. 12. Dose dependences of: the total number of precipitates N_p with the number of radiation induced precipitates N_p^* (in inset) (*a*); mean precipitate radius $\langle R_p \rangle$ of all precipitates with mean radius of radiation induced ones $\langle R_p^* \rangle$ shown in inset (*b*) [75]

of vacancies, precipitate dissolution is favoured. With the accumulation of a higher dose, we observe an increasing trend in N_p and $\langle R_p \rangle$, driven by radiation-enhanced diffusion and ballistic mixing. In Figure 12, *a*, we can observe that at $T = 550$ K and an elevated dose rate ($K = 10^{-6}$ dpa/s), the total number of all precipitates (with a radius larger than l and a niobium content of over 70%) increases after a certain incubation dose (approximately 0.8 dpa) [44]; precipitates with a radius smaller than l are not considered. At a higher temperature (the curve at T = 570 K, $K = 10^{-6}$ dpa/s), the number of precipitates is less than that at $T = 550$ K with the same dose rate. When the dose rate is reduced, the number of precipitates decreases due to a lower flux of defects, which regulates atomic diffusion and ballistic mixing (compare the curves at T = 550 K and different K values). The dynamics of the number of radiation-induced precipitates, N_p^*, are shown in the inset of Fig. 12, *a*. It is evident that at an elevated dose rate, the precipitation process begins at a low

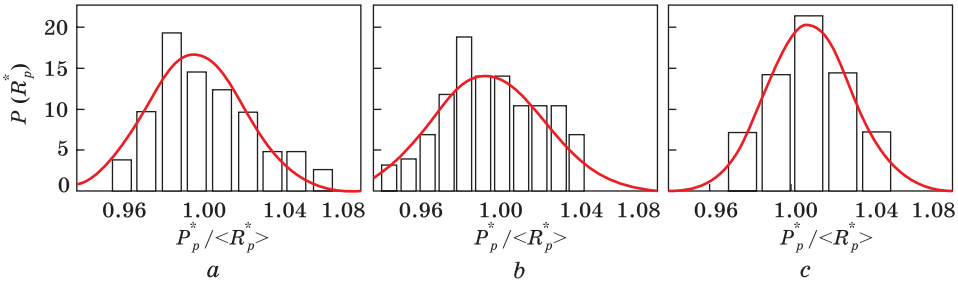

Fig. 13. Histograms of the precipitate size distribution at different irradiation conditions at 6 dpa: T = 550 K, $K = 5\times10^{-7}$ dpa/s, solid line relates to the lognormal fit (*a*); T = 550 K, $K = 10^{-6}$ dpa/s, solid line relates to the lognormal fit (*b*); T = 570 K, $K = 10^{-6}$ dpa/s, solid line relates to the Gaussian (normal) fit (*c*) [75] Snapshots are shown at different doses: 1 dpa (*a*), 2 dpa (*b*). Microstructure of the irradiated alloy with vacancy field at 1 dpa (*c*). Two-dimensional snapshots of Nb and vacancy concentration fields at 2 dpa (*d*) [75]

radiation dose, whereas at a lower dose rate and elevated temperature, precipitation starts at higher doses. In Figure 12, *b*, it is apparent that new precipitates with a size of approximately l emerge after an incubation dose of around 0.8 dpa. Here, the dissolution changes with the precipitation of new precipitates, where the material for these new precipitates is taken from the remaining niobium concentration in the matrix and additional concentration from the dissolved precipitates. The size of the new precipitates is smaller at higher dose rates compared to the size obtained at lower doses. At the same time, the density of the number of precipitates is higher at higher dose rates. A similar trend is observed with increasing irradiation temperature.

The results indicate that increasing the irradiation temperature and decreasing the dose rate have a similar effect. This effect is explained by the competition between ballistic mixing, responsible for the instability of a homogeneous configuration in the matrix with low niobium concentration, and the thermodynamic force that suppresses this instability, as shown in previous studies (see Refs. [48, 51]).

Calculated values of the density of precipitates and the average radius of radiation-induced precipitates in the quasi-stationary regime are $N_p \approx 10^{14}$ cm^{-3}, $R_p^* \approx 12$ nm at T = 550 K, $K = 10^{-6}$ dpa/s; $N_p^* \approx 4.1\times10^{13}$ cm^{-3}, $R_p^* \approx 13$ nm at T = 550 K, $K = 5\times10^{-7}$ dpa/s; $N_p^* \approx 7\times10^{13}$ cm^{-3}, $R_p^* \approx 14$ nm at T = 570 K, $K = 10^{-6}$ dpa/s. These obtained values are in good agreement with experimental observations discussed in the referenced papers [12, 44, 45]. Additionally, the results align well with experimental data from the OSIRIS reactor (CEA, Saclay, France), where an increase in the minimum precipitate size from 6 nm to 18 nm was observed at doses of 18 dpa with a density of approximately 10^{14}cm^{-3} (see Ref. [14]).

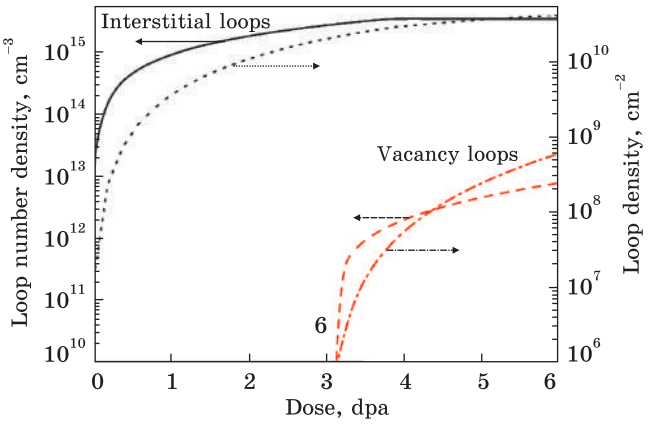

Fig. 14. Dose dependences of interstitial and vacancy type dislocation loop densities at T = = 550 K, $K = 10^{-6}$ dpa/s [75]

The statistical size distribution of precipitates under different irradiation conditions is presented in Fig. 13. Several key differences in the properties of the size distribution functions between the non-irradiated and irradiated systems should be highlighted. Firstly, this difference is due to the low dispersion of distributions for irradiated systems. In these cases, most particles have sizes close to the average. Secondly, the shape of the distributions for non-irradiated and irradiated systems differs. In the case of a system irradiated at a low dose rate (Fig. 13, *a*), the size distribution function exhibits a tail for $R_p^* > \langle R_p^* \rangle$ (fitted by a lognormal distribution represented by the solid curve). The dispersion of the corresponding lognormal distribution increases to 36% when the dose rate is elevated (see Fig. 13, *b*). This increase is attributed to the emergence of additional spatial instabilities caused by intensified ballistic mixing at higher dose rates. This is accompanied by a higher probability of the existence of small precipitates (with $R_p^* < \langle R_p \rangle$) and a lower probability of the existence of large precipitates (with $R_p^* > \langle R_p^* \rangle$) at the same dose. With increasing temperature (see Fig. 13, *b*, *c*), the size distribution function becomes more symmetrical. It is well approximated by a Gaussian distribution. The results indicate that raising the temperature leads to a reduction in the dispersion of the distribution centred on $R_p^* \approx \langle R_p^* \rangle$, which is different from the previous cases. Therefore, the change in the shape of the distribution function is associated with the competition between ballistic mixing and thermal diffusion, resulting in the formation and growth of new precipitates in the presence of the growth/dissolution of existing precipitates.

The typical dynamics of the density of interstitial and vacancy loops is shown in Fig. 14. Here, the density of interstitial loops increases to 3×10^{15} cm^{-3}, while the density of vacancy loops reaches values up to 10^{13} cm^{-3}. At 6 dpa, the density of interstitial loops increases approximately to 8×10^{10} cm^{-2}, and the density of vacancy loops is around

7×10^8 cm^{-2}. These results are in good agreement with the majority of experimental observations [12, 45, 132].

3.2.3. A Hardening Estimation

As known, formed dislocation loops and precipitates act as sinks for the movement of dislocations, leading to radiation hardening of irradiated materials. Using the obtained data, we can to assess the change in the mechanical properties of the studied system.

The increase in shear stress, $\Delta\tau_{tot}$, required to detach dislocations from sinks determines the yield strength increment $\Delta\sigma_Y^{tot} = M_{Zr}\Delta\tau_{tot}$, where $M_{Zr} = 3.5$ is the Taylor factor [133, 134]. In our case, the total hardening due to sinks is described by the increase in shear stresses [135]: $\Delta\tau_{tot} = (\Delta\tau_L^2 + \Delta\tau_p^2)^{1/2}$, where $\Delta\tau_L$ pertains to interstitial dislocations and $\Delta\tau_p$ corresponds to precipitates. Contributions from dislocation network and grain boundaries are not considered here. To compute the total increment in yield strength $\Delta\sigma_Y^{tot}t$, we use the average size of all possible precipitates and the corresponding total number density in the definitions for $\Delta\tau_p$ [136]: $\Delta\tau_p = \alpha_p\mu b\sqrt{2\langle R_p\rangle N_p}$, $\alpha_p = -0.85\alpha_{0p}\dfrac{\langle F\rangle}{2\pi}\ln(2b\sqrt{2\langle R_p\rangle N_p})$, where α_p is the barrier strength [137]. Here, the coefficient 0.85 takes into account the random distribution of sinks, $\alpha_{0p} \cong 0.1$, $\langle F\rangle = 1.25$. Strengthening due to dislocation loops is described by a dispersion-hardening model [138]. For interstitial dislocation loops in one direction, we have: $\Delta\tau_L = \alpha_L\mu b\sqrt{\rho_L/\pi}$, $\alpha_L = -0.85\alpha_{0L}\dfrac{\langle F\rangle}{2\pi}\ln(2b\sqrt{\rho_L/\pi})$, where $\alpha_{0L} \simeq$ $\simeq 0.2$, $\rho_L = 3\rho_I + \rho_V$ is the total density of dislocation loops, including all crystallographic directions, and $b = (b_a + b_c)/2$. To calculate the increment in yield strength due to radiation-induced precipitates, $\Delta\sigma_{Yp}^*$, we use $\Delta\tau_p^*$ and α_p^*, redefined as $\langle R_p^*\rangle$ and N_p^*.

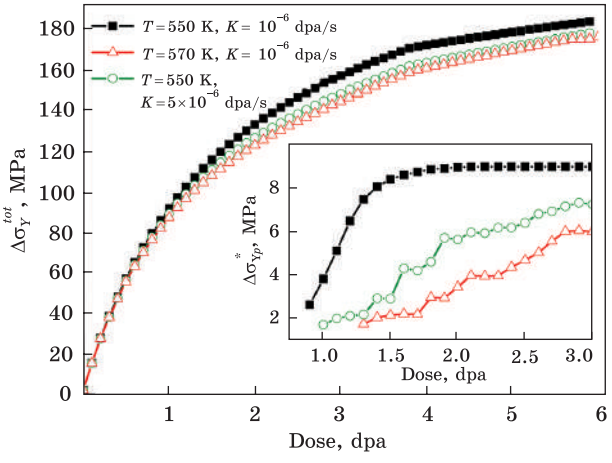

Fig. 15. Dose dependences of hardening at different irradiation conditions and a contribution to the hardening related to radiation induced precipitates in inset [75]

The corresponding dose dependences for the total yield strength increment and the yield strength increment induced by radiation-induced precipitates are shown in Fig. 15. The primary contribution to the overall strengthening is due to the growth of dislocation loops during irradiation, leading to dose dependences up to 185 MPa at 6 dpa in the reactor conditions. The strengthening due to radiation-induced precipitates, $\Delta\sigma_{Yp}^{*}$, presented in the inset, indicates an increase in the yield strength increment to 8.6 MPa under low-temperature and high-dose rate conditions. With increasing temperature or decreasing dose rate, lower values of $\Delta\sigma_{Yp}^{*}$ component are observed. The values of the yield strength increment are in good agreement with experimental observations [45].

3.3. Modelling Radiation-Induced Precipitation in Ternary Zr–Nb–Sn Alloys

In this section, we present the results of calculations for the ternary alloys Zr–2% Nb–0.5% Sn and Zr–0.4% Nb–0.5% Sn under neutron irradiation. The modelling is carried out in two stages. First, the sample is prepared by heat treatment of the solid solution, where the system's dynamics are determined only by diffusion fluxes. Here, we model the formation of nanosized β-Nb particles in the α-Zr matrix and the local rearrangement of lead atoms and equilibrium vacancies. In the next stage, using this microstructure as a target, we investigate radiation-induced precipitation of precipitates and the dissolution of pre-existing precipitates. Here, radiation-induced atomic mixing and the dynamics of the relevant non-equilibrium defects are considered together with thermodynamic flows.

We conducted the annealing of the Zr–2% Nb–0.5% Sn alloy at a temperature of 570 K. As the initial configuration, we took a solid solution with a random distribution of concentrations and average values for all elements: $\langle c_{\mathrm{Nb}}\rangle = 0.02$, $\langle c_{\mathrm{Sn}}\rangle = 0.005$, $\langle c_v\rangle = c_{v0}$. The system's dynamics are described by equations (8), and the concentration of zirconium is determined according to the law of mass conservation. In Figure 16, *a*, *b*, a typical microstructure formed during heat treatment is presented. As we can see, β-Nb precipitates are surrounded by vacancies, whose concentration exceeds the equilibrium value. This distribution of vacancy concentration is related to different types of interaction of niobium and zirconium atoms with vacancies in the thermodynamic potential. This implies that the concentration of vacancies in the β-phase is lower than the equilibrium value. The concentrations of vacancies and niobium in the α-phase are distributed almost uniformly. The annealing duration was 1450 hours. Precipitates larger than 5 nm were observed approximately 50 hours after annealing. Most precipitates have a spherical shape with slight anisotropy and contain about 75% niobium. The

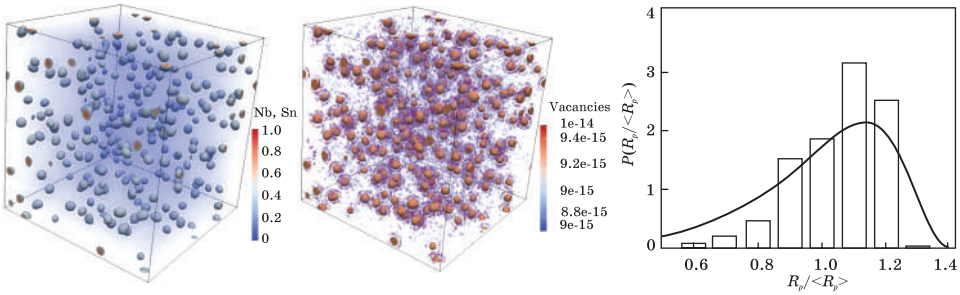

Fig. 16. Snapshots of β-Nb precipitates and local distribution of Sn concentration (*a*) and β-Nb precipitates surrounded by vacancies with concentration exceeding equilibrium value (*b*). Precipitate size distribution function (*c*) [77]

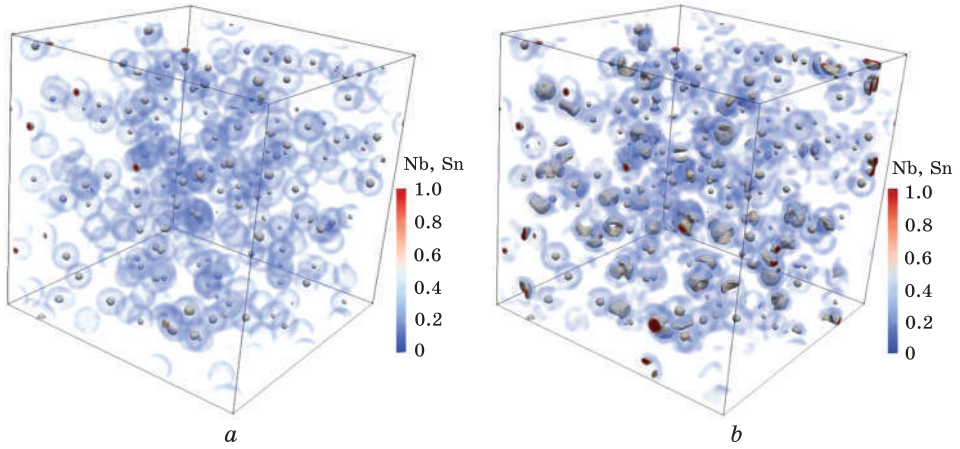

Fig. 17. Snapshots of microstructure at irradiation: 0.1 dpa (*a*) and 2.0 dpa (*b*) [77]

average radius of the precipitate $\langle R_p \rangle$ is approximately 13 nm; the density of precipitates is of 5×10^{14} cm^{-3} that is consistent with most experimental data [12]. A statistical analysis of the precipitate size distribution follows the Lifshitz–Slyozov–Wagner distribution (see Fig. 16, *c*). As in the case of the binary alloy Zr–2% Nb, a more accurate approximation is provided using the Marqusee and Ross approach. Here, we also assume that during the coarsening process, no nucleation or coalescence of particles occurs.

The prepared target is irradiated at the same temperature with a dose rate of $K = 10^{-6}$ dpa/s. The overall dynamics of the system during irradiation are described by a set of Eqs. (13)–(18) using expressions (9) and (10). The dislocation density is 10^{12} cm^{-2}. A typical scenario of microstructure evolution under irradiation is shown in Fig. 17. It can be observed that precipitate sizes are smaller at lower doses (Fig. 17, *a*).

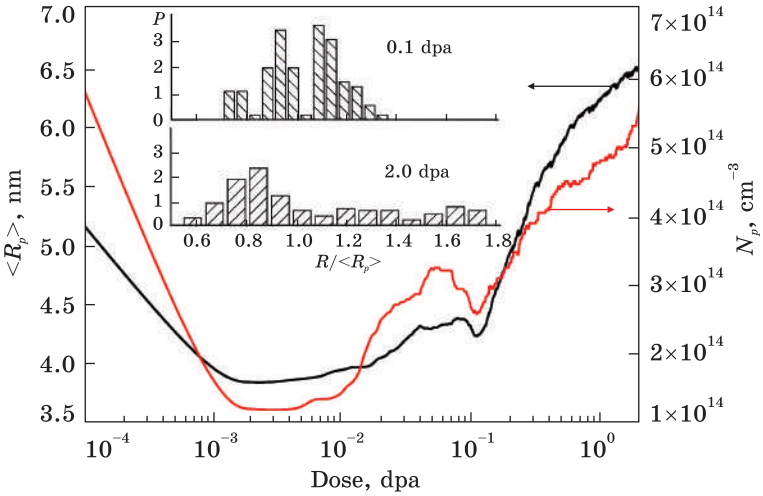

Fig. 18. Dose dependences of the mean precipitate size and precipitate number density. Histograms of size distributions are shown in the inset at different doses [77]

This is due to the dissolution of previously existing precipitates and the formation of small β-Nb clusters at low doses. As the dose accumulates, radiation-induced precipitation of precipitates occurs with an increasing number of precipitates. The concentration of tin locally increases in regions enriched with vacancies. Such behaviour of tin concentration is related to the trapping of vacancies by tin atoms. The most out-of-equilibrium vacancies are concentrated in areas enriched with tin atoms, away from the β-Nb precipitates.

The dose-dependent changes in the average radius of precipitates $\langle R_p \rangle$ and their number density N_p are presented in Fig. 18. As you can see, the dissolution of existing precipitates is accompanied by a reduction in their average size and number density. The precipitation of radiation-induced precipitates occurs at doses greater than 0.1 dpa, where the precipitate radius increases according to a power law as $(Kt)^{0.23}$. The number density of precipitates N_p shows a slow increasing trend. The average size increases to about 13 nm at doses around 2 dpa, while their density increases to 5×10^{14} cm^{-3}. These values for the average size of precipitates and their number density correlate with experimental observations collected in the study [12]. Histograms of the precipitate size distribution at different doses are shown in the inset of Fig. 18. Here, at low doses, the distribution closely resembles a normal distribution, while, at higher doses, it approaches a lognormal distribution. This is consistent with experimental data on precipitate size distributions [47]. In the studied scenario, we observe the precipitation of new precipitates as atoms are displaced from the surface of pre-existing precipitates due

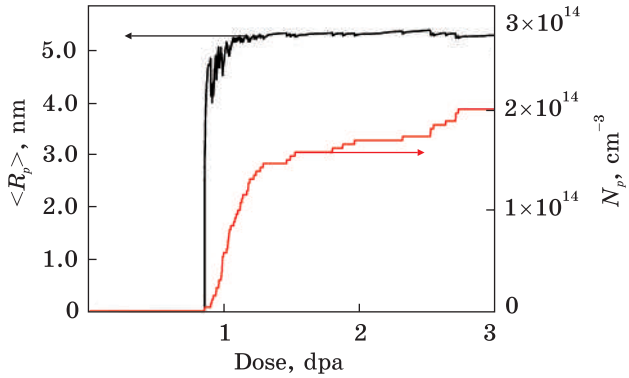

Fig. 19. Dose dependences of the mean precipitate size and precipitate number density [77]

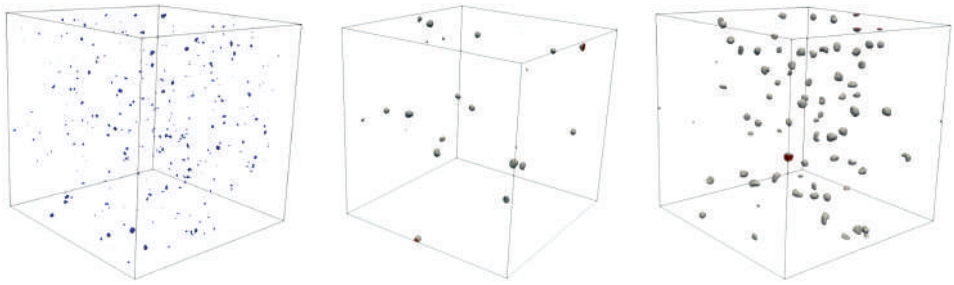

a *b* *c*

Fig. 20. Snapshots of microstructure at irradiation of Zr–0.4% Nb–0.5% Sn alloy: 0.8 dpa (*a*), 1.2 dpa (*b*), 3 dpa (*c*) [77]

to cascade mixing. These displaced atoms redistribute within the matrix and aggregate into new precipitates through radiation-stimulated diffusion by establishing new equilibrium conditions with the newly formed precipitates. This process leads to the formation of new precipitates and the reconfiguration of the microstructure in response to irradiation.

In this model, all precipitates contain approximately 80% niobium, while the rest of the niobium is distributed within the matrix. Under normal conditions, the niobium atoms dissolved in the matrix cannot form new precipitates. This only becomes possible when non-equilibrium defects created during irradiation enhance the diffusion of the solute. To investigate this effect, we examine the radiation-induced precipitation of precipitates in the highly soluble alloy Zr–0.4% Nb–0.5% Sn. Based on the results of the thermal treatment stage, we consider that 20% of the niobium resides in the matrix, dissolved between the precipitates of the β-phase in Zr–2% Nb–0.5% Sn. As the initial configuration for the part of the alloy between the precipitates, we choose a niobium concentration of 20%, which corresponds to 2% of the total niobium content in this alloy. Therefore, we are examining the Zr–0.4% Nb–0.5% Sn alloy. Initially, we randomly distribute both alloying com-

ponents within the zirconium matrix (similar to the thermal treatment stage), and then we model the influence of irradiation. The results obtained are presented in Figs. 19 and 20. Clearly, precipitates emerge after an incubation dose of approximately 0.8 dpa (see Fig. 19). Their quantity increases as the dose accumulates, and the average size slowly decreases after a dose of 2 dpa, which is related to the increased dynamics of their number density. In this case, the precipitates appear in the form of clusters due to radiation-stimulated diffusion and grow to a size of 10–11 nm with a density of 2×10^{14} cm^{-3} at doses up to 3 dpa. The obtained values for the precipitate size and their number density align well with experimental observations of the studied alloys [12, 47]. Thus, by employing such modelling, it is demonstrated that radiation-stimulated diffusion can initiate the precipitation processes in soluble systems.

4. Conclusions

An efficient approach for modelling the precipitation processes of secondary phase precipitates during thermal treatment and radiation-induced precipitation of new precipitates in binary and ternary alloys with low alloying element content and concentration-dependent mobilities has been proposed. The developed phase-field model is based on the CALPHAD approach, utilizing a thermodynamic potential database for all alloy components and including non-equilibrium vacancies. The structural disorder generated during irradiation is represented by introducing ballistic mixing with a fixed atomic displacement value, which is in accordance with previous modifications of the phase-field approach.

The modelling algorithm was employed to investigate the dynamics of β-phase precipitate formation in a model of the commercial Zr–1%Nb–1%Sn alloy during thermal treatment. Local rearrangements of the alloying elements and defect concentrations with different interaction types were studied. In the investigated alloy, it was found that β-phase precipitates begin to form after approximately 70 hours of annealing at a fixed temperature. It was demonstrated that the non-uniform distribution of vacancies in the volume results in non-uniform distribution of tin, which acts as vacancy traps, while β-Nb precipitates contain an extremely low concentration of vacancies due to mutual repulsion interactions. The analysis of the precipitation process revealed a trend in the precipitate size approaching a stable value over time, driven by the low alloying element content, excluding coalescence. The estimation of the yield strength increase due to β-phase precipitates was shown to increase over annealing time and precipitate size. Modelling the mechanical loads in the form of shear deformation of the annealed alloy in the presence of precipitates revealed that an increase in the de-

formation rate leads to an increase in the corresponding values of yield strength and strength.

It was shown that during the development of plastic deformation, dislocation loops are formed due to the slip around interphase boundaries. Solid precipitates confine loop segments near precipitates, while segments outside precipitates, following the Orowan's mechanism, grow into a softer (matrix) phase. The interaction between 'dislocation loop–precipitate' was found to be determined by the difference in the elastic moduli of the matrix phase and the precipitate phase.

In the context of the proposed approach, competing mechanisms responsible for microstructural transformations in the binary Zr–2% Nb system under neutron irradiation were also investigated. The model simulated the precipitation of β-phase precipitates during thermal treatment, their dissolution, and radiation-induced precipitation under reactor conditions. The obtained results extend previous research on microstructural transformations in Zr–Nb alloys. The time scales of the appearance of well-defined precipitates during annealing and the incubation dose for the formation of radiation-induced precipitates qualitatively agree with experimental observations. The local distribution of non-equilibrium vacancies around β precipitates corresponds to atomistic simulations and can be used to interpret positron-annihilation results for Zr–Nb alloys. The dynamics and statistical properties of precipitate dissolution in unirradiated and radiation-induced conditions were studied. A joint consideration of precipitation kinetics with point defect sinks was used to estimate the strengthening of the irradiated alloy, quantitatively and qualitatively consistent with experimental observations.

Moreover, as a model system under irradiation, the ternary Zr–2% Nb–0.5% Sn alloy was investigated. It was shown that vacancies with concentrations exceeding their equilibrium value accumulate at phase boundaries, leading to the smearing of tin atom concentrations within the volume with some segregation at interphase boundaries. During irradiation, most non-equilibrium vacancies and tin atoms are concentrated at the phase boundaries, related to the trapping of vacancies by tin atoms. Precipitate re-precipitation processes during irradiation occur through the dissolution of existing precipitates and the formation of new ones from the atomic supply due to the structural disorder. The difference in the shape of the precipitate size distribution functions for samples before and after irradiation indicates a more complex nature of the radiation-induced precipitation process compared to the standard precipitation scenario during annealing. As shown, this process begins after an incubation dose due to the competition between diffusion and ballistic mixing.

The obtained results are consistent with experimental observations under corresponding conditions and can be used to predict material behaviour under annealing, irradiation, and mechanical loads.

REFERENCES

1. Y.H. Jeong, K.O. Lee, and H.G. Kim, *J. Nucl. Mater.*, **302**, Iss. 1: 9 (2002); https://doi.org/10.1016/S0022-3115(02)00703-1
2. H.G. Kim, J.Y. Park, and Y.H. Jeong, *J. Nucl. Mater.*, **347**, Iss. 1–2: 140 (2005); https://doi.org/10.1016/j.jnucmat.2005.08.008
3. P. Cirimello, G. Domizzi, and R. Haddad, *J. Nucl. Mater.*, **350**, Iss. 2: 135 (2006); https://doi.org/10.1016/j.jnucmat.2005.12.002
4. C.P. Ramos, M.S. Granovsky, and C. Saragovi, *Physica B*, **389**, Iss. 1: 67 (2007); https://doi.org/10.1016/j.physb.2006.07.026
5. G. Choudhuri, Jagannath, M.K. Kumar, V. Kain, D. Srivastava, S. Basu, B.K. Shah, N. Saibaba, and G. K. Dey, *J. Nucl. Mater.*, **441**, Iss. 1–3: 178 (2013); https://doi.org/10.1016/j.jnucmat.2013.05.026
6. M. Ito, K. Ko, H. Muta, M. Uno, and S. Yamanaka, *J. Alloys Compd.*, **446**: 451 (2007); https://doi.org/10.1016/j.jallcom.2007.01.084
7. T. Toyama, Y. Matsukawa, K. Saito, Y. Satoh, H. Abe, Y. Shinohara, and Y. Nagai, *Scr. Mater.*, **108**: 156 (2015); https://doi.org/10.1016/j.scriptamat.2015.07.005
8. V.N. Shishov, M.M. Peregud, A.V. Nikulina, Y.V. Pimenov, G.P. Kobylyansky, A.E. Novoselov, Z.E. Ostrovsky, and A.V. Obukhov, *J. ASTM Int.*, **2**, Iss. 8: JAI12431 (2005); https://doi.org/10.1520/JAI12431
9. S. Doriot, D. Gilbon, J.L. Béchade, M.H. Mathon, L. Legras, and J.P. Mardon, *J. ASTM Int.*, **2**, Iss.7: JAI12332 (2005); https://doi.org/10.1520/JAI12332
10. V.N. Shishov, A.V. Nikulina, V.A. Markelov, M.M. Peregud, A.V. Kozlov, S.A. Averin, S.A. Kolbenkow, and A.E. Novoselov, *Zirconium in the Nuclear Industry: 11th Int. Symp.* (Eds. E. R. Bradley and G. P. Sabol) (West Conshohocken, PA: ASTM STP: 1996), vol. **1295**, p. 603; https://doi.org/10.1520/STP16192S
11. C.D. Cann, C.B. So, R.C. Styles, and C.E. Coleman, *J. Nucl. Mater.*, **205**: 267 (1993); https://doi.org/10.1016/0022-3115(93)90089-H
12. F. Onimus and J. L. Béchade, *Comprehensive Nuclear Materials* (Ed. R.J. M. Konings) (Oxford: Elsevier: 2012), vol. **4**, p. 1; https://doi.org/10.1016/B978-0-08-056033-5.00064-1
13. G. He, J. Liu, K. Li, J. Hu, A.H. Mir, S. Lozano-Perez, and C. Grovenor, *J. Nucl. Mater.*, **526**: 151738 (2019); https://doi.org/10.1016/j.jnucmat.2019.151738
14. Q. Dong, Z. Yao, Q. Wang, H. Yu, M.A. Kirk, and M.R. Daymond, *Metals*, **7**, Iss. 8: 287 (2017); https://doi.org/10.3390/met7080287
15. T. Andersson and G. Vesterlund, *Zirconium in the Nuclear Industry: 5th Int. Symp.* (Philadelphia: ASTM STP: 1982), vol. **754**, p. 75.
16. T. Andersson and T. Thorvaldsson, *Zirconium in the Nuclear Industry: 7th Int. Symp.* (Eds. R. B. Adamson and L. F. P. Van Swam) (Philadelphia: ASTM STP: 1987), vol. **939**, p. 321; https://doi.org/10.1520/STP28131S
17. B. Cheng and R.B. Adamson, *Zirconium in the Nuclear Industry: 7th Int. Symp.* (Eds. R.B. Adamson and L.F.P. Van Swam) (Philadelphia: ASTM STP: 1987), vol. **939**, p. 387; https://doi.org/10.1520/STP28134S

18. R. M. Kruger, R. B. Adamson, and S. S. Brenner, *J. Nucl. Mater.*, **189**, Iss. 2: 193 (1992);
https://doi.org/10.1016/0022-3115(92)90532-P
19. T. Kubo and M. Uno, *Zirconium in the Nuclear Industry: 9th Int. Symp.* (Eds. C.M. Eucken and A.M. Garde) (Philadelphia: ASTM STP: 1991), vol. **1132**, p. 476;
https://doi.org/10.1520/STP25523S
20. G. Maussner, E. Steinberg, and E. Tenckhoff, *Zirconium in the Nuclear Industry: 7th Int. Symp.* (Eds. R.B. Adamson and L.F.P. Van Swam) (Philadelphia: ASTM STP: 1987), vol. **939**, p. 307.
https://doi.org/10.1520/STP28130S
21. R. Krishnan and M. K. Asundi, *Proc. Indian Acad. Sci. (Eng. Sci.)*, **4**: 41 (1981);
https://doi.org/10.1007/BF02843474
22. S.C. Lumley, S.T. Murphy, P.A. Burr, R.W. Grimes, P.R. Chard-Tuckey, and M.R. Wenman, *J. Nucl. Mater.*, **437**, Iss. 1–3: 122 (2013);
https://doi.org/10.1016/j.jnucmat.2013.01.335
23. L. Wu, V.O. Kharchenko, D.O. Kharchenko, and R. Pan, *Mater. Today Commun.*, **26**: 101765 (2021);
https://doi.org/10.1016/j.mtcomm.2020.101765
24. Z. Yu, X. Xu, A. Mansoor, B. Du, K. Shi, K. Liu, S. Li, and W. Du, *J. Mater. Sci. Technol.*, **88**: 21 (2021);
https://doi.org/10.1016/j.jmst.2021.01.070
25. R. Liu, D.L. Yin, and J.T. Wang, *Magnesium Technology 2012* (Eds. S.N. Mathaudhu, W.H. Sillekens, N.R. Neelameggham, and N. Hort) (Cham: Springer: 2012), p. 555;
https://doi.org/10.1007/978-3-319-48203-3_98
26. W. Cai, J. Zhang, Z.Y. Gao, and J.H. Sui, *Appl. Phys. Lett.*, **92**: 252502 (2008);
https://doi.org/10.1063/1.2943661
27. J.W. Cahn, *Acta Metall.*, **9**: 795 (1961);
https://doi.org/10.1016/0001-6160(61)90182-1
28. J.W. Cahn, *Acta Metall.*, **10**: 179 (1962);
https://doi.org/10.1016/0001-6160(62)90114-1
29. J.W. Cahn and J.E. Hilliard, *Acta Metall.*, **19**: 151 (1971);
https://doi.org/10.1016/0001-6160(71)90127-1
30. A.G. Khachaturyan, *Theory of Structural Transformations in Solids* (Courier Corporation: 2013).
31. L.Q. Chen, *Acta Metall. Mater.*, **42**, Iss. 10: 3503 (1994);
https://doi.org/10.1016/0956-7151(94)90482-0
32. S.G. Kim, W.T. Kim, and T. Suzuki, *Phys. Rev. E*, **60**: 7186 (1999);
https://doi.org/10.1103/PhysRevE.60.7186
33. L.Q. Chen, *Annu. Rev. Mater. Res.*, **32**: 113 (2002);
https://doi.org/10.1146/annurev.matsci.32.112001.132041
34. N. Moelans, B. Blanpain, and P. Wollants, *CALPHAD*, **32**, Iss. 2: 268 (2008);
https://doi.org/10.1016/j.calphad.2007.11.003
35. K. Wu, S. Chen, F. Zhang, and Y.A. Chang, *J. Phase Equilib. Diffus.*, **30**: 571 (2009);
https://doi.org/10.1007/s11669-009-9567-1
36. I. Loginova, J. Odqvist, G. Amberg, and J. Agren, *Acta Mater.*, **51**, Iss. 5: 1327 (2003);
https://doi.org/10.1016/S1359-6454(02)00527-X
37. G. Choudhuri, S. Chakraborty, D. Srivastava, and G.K. Dey, *Results in Physics*, **3**: 7 (2013);
https://doi.org/10.1016/j.rinp.2012.12.003

38. G.S. Was, *Fundamentals of Radiation Materials Science* (Berlin–Heidelberg: Springer-Verlag: 2007).
39. K. Nuttall and D. Faulkner, *J. Nucl. Mater.*, **67**, Iss. 1–2: 131 (1977); https://doi.org/10.1016/0022-3115(77)90169-6
40. R.M. Kruger and R. B. Adamson, *J. Nucl. Mater.*, **205**: 242 (1993); https://doi.org/10.1016/0022-3115(93)90086-E
41. V. Perovic, A. Perovic, G. C. Weatherly, and G. R. Purdy, *J. Nucl. Mater.*, **224**, Iss. 1: 93 (1995); https://doi.org/10.1016/0022-3115(95)00044-5
42. C.E. Coleman, R.W. Gilbert, G.J.C. Carpenter, and G.C. Weatherly, *Proc. Phase Stability during Irradiation Symp.* (Eds. J.R. Holland, L.K. Mansur, and D.I. Potter) (New York: The Metallurgical Society of AIME: 1981), p. 587.
43. Q. Dong, H. Yu, Z. Yao, F. Long, L. Balogh, and M.R. Daymond, *J. Nucl. Mater.*, **481**: 153 (2016); https://doi.org/10.1016/j.jnucmat.2016.09.017
44. V.F. Urbanic and M. Griffiths, *Zirconium in the Nuclear Industry: 12th Int. Symp.* (Eds. G.P. Sabol and G.D. Moan) (Philadelphia: ASTM STP: 2000), vol. **1354**, p. 641; https://doi.org/10.1520/STP14321S
45. C. Song, *CNL Nuclear Review*, **5**, Iss. 1: 17 (2016); https://doi.org/10.12943/cnr.2016.00010
46. G. Monnet, *Philos. Mag.*, **86**, Iss. 36: 5927 (2006); https://doi.org/10.1080/14786430600860985
47. J. Ribis, *Comprehensive Nuclear Materials (2nd Ed.)* (Eds. R.J.M. Konings and R.E. Stoller) (Oxford: Elsevier: 2020), vol. **1**, p. 265; https://doi.org/10.1016/B978-0-12-803581-8.11647-9
48. P. Bellon, *Comprehensive Nuclear Materials* (Ed. R.J.M. Konings) (Oxford: Elsevier: 2012), vol. **1**, p. 411; https://doi.org/10.1016/B978-0-08-056033-5.00031-8
49. D.O. Kharchenko, V.O. Kharchenko, I.O. Lysenko, and I.A. Shuda, *Physica A*, **486**: 497 (2017); https://doi.org/10.1016/j.physa.2017.05.053
50. D.O. Kharchenko, V.O. Kharchenko, Y.M. Ovcharenko, O.B. Lysenko, I.A. Shuda, L. Wu, and R. Pan, *Condens. Matter. Phys.*, **21**, No. 1: 13002 (2018); https://doi.org/10.5488/CMP.21.13002
51. D.O. Kharchenko, V.O. Kharchenko, A.I. Bashtova, V.V. Kupriienko, and L. Wu, *J. Appl. Phys.*, **129**: 035104 (2021); https://doi.org/10.1063/5.0031917
52. S. Rokkam, A. El-Azab, P. Millett, and D. Wolf, *Modelling Simul. Mater. Sci. Eng.*, **17**: 064002 (2009). https://doi.org/10.1088/0965-0393/17/6/064002
53. D.O. Kharchenko and V.O. Kharchenko, *Radiat. Eff. Defects Solids*, **171**, Iss. 11–12: 819 (2016); https://doi.org/10.1080/10420150.2016.1274753
54. Y. Li, S. Hu, X. Sun, and M. Stan, *npj Comput. Mater.*, **3**: 16 (2017); https://doi.org/10.1038/s41524-017-0018-y
55. M.R. Tonks, A. Cheniour, and L. Aagesen, *Comput. Mater. Sci.*, **147**: 353 (2018); https://doi.org/10.1016/j.commatsci.2018.02.007
56. M.R. Tonks and L.K. Aagesen, *Annu. Rev. Mater. Res.*, **49**: 79 (2019); https://doi.org/10.1146/annurev-matsci-070218-010151

57. D.O. Kharchenko, O.M. Shchokotova, V.O. Kharchenko, V.V. Kupriienko, S.V. Kokhan, X. Wu, and L. Wu, *Radiat. Eff. Defects Solids*, **175**, Iss. 7–8: 602 (2020); https://doi.org/10.1080/10420150.2019.1684918
58. A. Onuki, *Phase Transition Dynamics* (Cambridge : Cambridge University Press: 2002); https://doi.org/10.1017/CBO9780511534874
59. A. Basak and V.I. Levitas, *Acta Mater.*, **189**: 255 (2020); https://doi.org/10.1016/j.actamat.2020.02.047
60. A. Basak and V.I. Levitas, *Comput. Meth. Appl. Mech. Eng.*, **343**: 368 (2019); https://doi.org/10.1016/j.cma.2018.08.006
61. N. Saunders and A. P. Miodownik, *CALPHAD (Calculation of Phase Diagrams): A Comprehensive Guide, Pergamon Materials Series* (Ed. R.W. Cahn) (Oxford: Pergamon: 1998), vol. **1**.
62. A.T. Dinsdale, *Calphad*, **15**, Iss. 4: 317 (1991); https://doi.org/10.1016/0364-5916(91)90030-N
63. Y. Li, S. Hu, C.H. Henager, H. Deng, F. Gao, X. Sun, and M.A. Khaleel, *J. Nucl. Mater.*, **427**, Iss. 1–3: 259 (2012); https://doi.org/10.1016/j.jnucmat.2012.05.004
64. P. C. Millett, S. Rokkam, A. El-Azab, M. Tonks, and D. Wolf, *Modelling Simul. Mater. Sci. Eng.*, **17**: 064003 (2009); https://dx.doi.org/10.1088/0965-0393/17/6/064003
65. Y.H. Wang, D.C. Zhang, Z. P. Pi, J.G. Lin, and C. Wen, *J. Appl. Phys.*, **126**: 085102 (2019); https://doi.org/10.1063/1.5096820
66. S.B. Biner, *Programming Phase-Field Modeling* (Cham: Springer: 2017); https://doi.org/10.1007/978-3-319-41196-5
67. S.I. Golubov, A.V. Barashev, and R.E. Stoller, *Comprehensive Nuclear Materials* (Ed. R.J.M. Konings) (Oxford: Elsevier: 2012), vol. **1**, p. 357; https://doi.org/10.1016/B978-0-08-056033-5.00029-X
68. A.V. Barashev, S.I. Golubov, and R.E. Stoller, *J. Nucl. Mater.*, **461**: 85 (2015); https://doi.org/10.1016/j.jnucmat.2015.02.001
69. A. Patra, C.N. Tomé, and S.I. Golubov, *Philos. Mag.*, **97**, Iss. 23: 2018 (2017); https://doi.org/10.1080/14786435.2017.1324648
70. R.A. Enrique and P. Bellon, *Phys. Rev. Lett.*, **84**: 2885 (2000); https://doi.org/10.1103/PhysRevLett.84.2885
71. R.A. Enrique and P. Bellon, *Phys. Rev. B*, **63**: 134111 (2001); https://doi.org/10.1103/PhysRevB.63.134111
72. R.A. Enrique, K. Nordlund, R.S. Averback, and P. Bellon, *J. Appl. Phys.*, **93**: 2917 (2003); https://doi.org/10.1063/1.1540743
73. R.A. Enrique and P. Bellon, *Phys. Rev. B*, **70**: 224106 (2004); https://doi.org/10.1103/PhysRevB.70.224106
74. G. Demange, L. Luneville, V. Pontikis, and D. Simeone, *J. Appl. Phys.*, **121**: 125108 (2017); https://doi.org/10.1063/1.4978964
75. V.O. Kharchenko, T. Xin, L. Wu, D.O. Kharchenko, V.V. Kupriienko, and I.O. Shuda, *Modelling Simul. Mater. Sci. Eng.*, **30**: 075006 (2022); https://doi.org/10.1088/1361-651X/ac8fad
76. V.O. Kharchenko, X. Kong, T. Xin, L. Wu, O. M. Shchokotova, D. O. Kharchenko, and S.V. Kokhan, *Phys. Scr.*, **98**, No. 3: 035714 (2023); https://doi.org/10.1088/1402-4896/acbcf9

77. V. Kharchenko, D. Kharchenko, V. Kupriienko, S. Kokhan, T. Xin, and L. Wu, *Proc. 2022 IEEE 12th Int. Conf. Nanomaterials: App. & Prop. (NAP) (Sep. 11–16, 2022, Krakow, Poland)* (IEEE: 2022), p. 1; https://doi.org/10.1109/NAP55339.2022.9934767
78. P.C. Hohenberg and B.I. Halperin, *Rev. Mod. Phys.*, **49**: 435 (1977); https://doi.org/10.1103/RevModPhys.49.435
79. J.D. Gunton, M.S. Miguel, and P. Sahni, *Phase Transitions and Critical Phenomena* (Eds. C. Domb and J.L. Lebowitz) (New York: Academic Press: 1983), vol. **8**, p. 267.
80. Y. Wang, L.Q. Chen, and A.G. Khachaturyan, *Computer Simulation in Materials Science Nano/Meso/Macroscopic Space & Time Scales* (Eds. H.O. Kirchner, K.P. Kubin, and V. Pontikis) (Dordrecht, the Netherlands: Kluwer Academic Publishers: 1996), p. 325.
81. Y. Wang and L.Q. Chen, *Methods in Materials Research* (Ed. E.N. Kaufmann) (New York: Wiley: 2000), p. 2a.3.1.
82. K. Wu, J.E. Morral, and Y. Wang, *Acta Mater.*, **49**, Iss. 17: 3401 (2001); https://doi.org/10.1016/S1359-6454(01)00257-9
83. C. Huang, M.O. de La Cruz, and B.W. Swift, *Macromolecules*, **28**: 7996 (1995); https://doi.org/10.1021/ma00128a005
84. A.A. Turkin and A.S. Bakai, *J. Nucl. Mater.*, **358**, Iss. 1: 10 (2006); https://doi.org/10.1016/j.jnucmat.2006.05.054
85. R.R. Mohanty, J.E. Guyer, and Y.H. Sohn, *J. Appl. Phys.*, **106**: 034912 (2009); https://doi.org/10.1063/1.3190607
86. M.J. Norgett, M.T. Robinson, and I.M. Torrens, *Nucl. Eng. Des.*, **33**, Iss. 1: 50 (1975); https://doi.org/10.1016/0029-5493(75)90035-7
87. J.H.Ke, E.R. Reese, E.A. Marquis, G.R. Odette, and D. Morgan, *Acta Mater.*, **164**: 586 (2019); https://doi.org/10.1016/j.actamat.2018.10.063
88. F.Kh. Mirzoev, V.Ya. Panchenko, and L.A. Shelepin, *Phys.-Usp.*, **39**: 1 (1996); https://doi.org/10.1070/pu1996v039n01abeh000125
89. D.O. Kharchenko, V.O. Kharchenko, A.I. Bashtova, and I.O. Lysenko, *Physica A*, **463**: 152 (2016); https://doi.org/10.1016/j.physa.2016.07.019
90. G.J.C. Carpenter, R.H. Zee, and A. Rogerson, *J. Nucl. Mater.*, **159**: 86 (1988); https://doi.org/10.1016/0022-3115(88)90087-6
91. A. Jostsons, P.M. Kelly, R.G. Blake, and K. Farrell, *Effects of Radiation on Structural Materials* (Eds. J.A. Sprague and D. Kramer) (ASTM STP: 1979), p. 46; https://doi.org/10.1520/STP38157S
92. S.R. MacEwen and G.J.C. Carpenter, *J. Nucl. Mater.*, **90**, Iss. 1–3: 108 (1980); https://doi.org/10.1016/0022-3115(80)90249-4
93. L.Q. Chen and J. Shen, *Comput. Phys. Commun.*, **108**, Iss. 2–3: 147 (1998); https://doi.org/10.1016/S0010-4655(97)00115-X
94. J.I. Ramos and C. Canuto, *Applied Mathematical Modelling* (New York: Springer-Verlag: 1988).
95. T. Korhonen, M.J. Puska, and R.M. Nieminen, *Phys. Rev. B*, **51**, Iss. 15: 9526 (1995); https://doi.org/10.1103/PhysRevB.51.9526
96. F. Legrain and S. Manzhos, *AIP Adv.*, **6**, Iss. 4: 045116 (2016); https://doi.org/10.1063/1.4948434
97. W.G. Wolfer, *Comprehensive Nuclear Materials* (Ed. R.J.M. Konings) (Oxford: Elsevier: 2012), vol. **1**, p. 1; https://doi.org/10.1016/B978-0-08-056033-5.00001-X

98. E.S. Fisher and C.J. Renken, *Phys. Rev.*, **135**: A482 (1964); https://doi.org/10.1103/PhysRev.135.A482
99. Y.J. Hao, L. Zhang, X.R. Chen, Y.H.Li, and H.L. He, *J. Phys.: Condens. Matter.*, **20**: 235230 (2008); https://doi.org/10.1088/0953-8984/20/23/235230
100. G. Simmons and H. Wang, *Single Crystal Elastic Constants and Calculated Aggregate Properties: A Handbook* (Cambridge: MIT Press: 1971).
101. S.N. Vaboya and G.C. Kennedy, *J. Phys. Chem. Solids*, **31**, Iss. 10: 2329 (1970); https://doi.org/10.1016/0022-3697(70)90247-7
102. P.F. Weck, E. Kim, V. Tikare, and J.A. Mitchell, *Dalton Trans.*, **44**: 18769 (2015); https://doi.org/10.1039/C5DT03403E
103. A.C.P. Jain, P.A. Burr, and D.R. Trinkle, *Phys. Rev. Materials*, **3**: 033402 (2019); https://doi.org/10.1103/PhysRevMaterials.3.033402
104. F. Christien and A. Barbu, *J. Nucl. Mater.*, **346**, Iss. 2–3: 272 (2005); https://doi.org/10.1016/j.jnucmat.2005.06.024
105. J. García-Ojalvo and J.M. Sancho, *Noise in Spatially Extended Systems* (New York: Springer: 1999); https://doi.org/10.1007/978-1-4612-1536-3
106. B. Holmedal, *Philos. Mag. Lett.*, **95**, Iss. 12: 594 (2015); https://doi.org/10.1080/09500839.2015.1125029
107. J.D. Robson, *J. Nucl. Mater.*, **377**, Iss. 3: 415 (2008); https://doi.org/10.1016/j.jnucmat.2008.03.016
108. I.M. Lifshitz and V.V. Slyozov, *J. Phys. Chem. Solids*, **19**, Iss. 1–2: 35 (1961); https://doi.org/10.1016/0022-3697(61)90054-3
109. C. Wagner, *Z. Elektrochem*, **65**, Iss. 7–8: 581 (1961); https://doi.org/10.1002/bbpc.19610650704
110. W.D. Callister, Jr. and D.G. Rethwisch, *Fundamentals of Materials Science and Engineering: An Integrated Approach* (Wiley: 2012).
111. D.J. Bacon, U.F. Kocks, and R.O. Scattergood, *Philos. Mag.*, **28**, Iss. 6: 1241 (1973); https://doi.org/10.1080/14786437308227997
112. A. Lehtinen, L. Laurson, F. Granberg, K. Nordlund, and M.J. Alava, *Sci. Rep.*, **8**: 6914 (2018); https://doi.org/10.1038/s41598-018-25285-z
113. B. Kombaiah and K.L. Murty, *Metall. Mater. Trans. A*, **46**: 4646 (2015); https://doi.org/10.1007/s11661-015-3060-8
114. A. Onuki, *Phys. Rev. E*, **68**: 061502 (2003); https://doi.org/10.1103/PhysRevE.68.061502
115. A. Minami and A. Onuki, *Phys. Rev. B*, **70**: 184114 (2004); https://doi.org/10.1103/PhysRevB.70.184114
116. A. Minami and A. Onuki, *Phys. Rev. B*, **72**: 100101 (2005); https://doi.org/10.1103/PhysRevB.72.100101
117. A. Onuki, A. Furukawa, and A. Minami, *Pramana – J. Phys.*, **64**: 661 (2005); https://doi.org/10.1007/BF02704575
118. A. Minami and A. Onuki, *Acta Mater.*, **55**, Iss. 7: 2375 (2007); https://doi.org/10.1016/j.actamat.2006.11.030
119. S.Y. Hu and L. Q. Chen, *Acta Mater.*, **49**, Iss. 11: 1879 (2001); https://doi.org/10.1016/S1359-6454(01)00118-5
120. V.A. Serbenta, N.V. Skripnyak, V.A. Skripnyak, and E.G. Skripnyak, *AIP Conf. Proc.*, **1909**: 020190 (2017); https://doi.org/10.1063/1.5013871

121. M.F. Horstemeyer, M.I. Baskes, and S.J. Plimpton, *Acta Mater.*, **49**, Iss. 20: 4363 (2001);
https://doi.org/10.1016/S1359-6454(01)00149-5
122. Z.L. Liu, X.C. You, and Z. Zhuang, *Int. J. Solids Struct.*, **45**, Iss. 13: 3674 (2008);
https://doi.org/10.1016/j.ijsolstr.2007.08.032
123. Y. Guo, Z. Zhuang, X.Y. Li, and Z. Chen, *Int. J. Solids Struct.*, **44**, Iss. 3–4: 1180 (2007);
https://doi.org/10.1016/j.ijsolstr.2006.06.008
124. W. Zhou, X. Ren, Y. Yang, Z. Tong, and L. Chen, *Int. J. Adv. Manuf. Technol.*, **108**: 1073 (2020);
https://doi.org/10.1007/s00170-019-04822-8
125. E. Schmid and W. Boas, *Plasticity of Crystals* (F.A. Hughes & Co.: 1950).
126. L.M. Brown and W.M. Stobbs, *Philos. Mag.*, **23**, Iss. 185: 1185 (1971);
https://doi.org/10.1080/14786437108217405
127. J.D. Atkinson, L.M. Brown, and W.M. Stobbs, *Philos. Mag.*, **30**, Iss. 6: 1247 (1974);
https://doi.org/10.1080/14786437408207280
128. H.G. Kim, Y.H. Jeong, and T.H. Kim, *J. Nucl. Mater.*, 326, Iss. 2–3: 125 (2004);
https://doi.org/10.1016/j.jnucmat.2004.01.015
129. A. Harte, M. Griffiths, and M. Preuss, *J. Nucl. Mater.*, **505**: 227 (2018);
https://doi.org/10.1016/j.jnucmat.2018.03.030
130. J.A. Marqusee and J. Ross, *J. Chem. Phys.*, **80**: 536 (1984);
https://doi.org/10.1063/1.446427
131. K.C. Russell, *KTG/BNES Conf. Irradiation Behaviour of Fuel Cladding and Core Component Materials* (Karlsruhe: 1974).
132. R.A. Holt, A.R. Causey, N. Christodoulou, M. Griffiths, E.T.C. Ho, and C.H. Woo, *Zirconium in the Nuclear Industry: 11th Int. Symp.* (Eds. E.R. Bradley and G.P. Sabol) (West Conshohocken, PA: ASTM STP: 1996), vol. **1295**, p. 623;
https://doi.org/10.1520/STP16193S
133. H.L. Yang, Y. Matsukawa, S. Kano, Z.G. Duan, K. Murakami, and H. Abe, *J. Nucl. Mater.*, **481**: 117 (2016);
https://doi.org/10.1016/j.jnucmat.2016.09.016
134. L. Chai, B. Luan, D. Xiao, M. Zhang, K.L. Murty, and Q. Liu, *Mater. Des.*, **85**: 296 (2015);
https://doi.org/10.1016/j.matdes.2015.06.088
135. R.C. Rau and J. Moteff, *Radiat. Eff.*, **8**, Iss. 1–2: 99 (1971);
https://doi.org/10.1080/00337577108231014
136. S. Kotrechko, V. Dubinko, N. Stetsenko, D. Terentyev, X. He, and M. Sorokin, *J. Nucl. Mater.*, **464**: 6 (2015);
https://doi.org/10.1016/j.jnucmat.2015.04.014
137. Y. Matsukawa, H.L. Yang, K. Saito, Y. Murakami, T. Maruyama, T. Iwai, K. Murakami, Y. Shinohara, T. Kido, T. Toyama, Z. Zhao, Y.F. Li, S. Kano, Y. Satoh, Y. Nagai, and H. Abe, *Acta Mater.*, **102**: 323 (2016);
https://doi.org/10.1016/j.actamat.2015.09.038
138. G.R. Odette and D. Frey, *J. Nucl. Mater.*, **85–86**: 817 (1979);
https://doi.org/10.1016/0022-3115(79)90360-X
139. L. Wu, V.O. Kharchenko, X. Kong, and D.O. Kharchenko, *J. Nucl. Mater.*, **554**: 153079 (2021);
https://doi.org/10.1016/j.jnucmat.2021.153079

Received 27.10.2023
Final version 04.02.2024

Д.О. Харченко[1], *В.О. Харченко*[1,2], *О.М. Щокотова*[1],
В.В. Купрієнко[1], *О.Б. Лисенко*[1], *С.В. Кохан*[1]

[1] Інститут прикладної фізики НАН України,
вул. Петропавлівська, 58,
40000 Суми, Україна

[2] Сумський державний університет,
вул. Римського-Корсакова, 2, 40007 Суми, Україна

МОДЕЛЮВАННЯ ПРЕЦИПІТАЦІЇ ВТОРИННОЇ ФАЗИ У КОМЕРЦІЙНИХ ЦИРКОНІЙОВИХ СТОПАХ ПІД ЧАС НЕЙТРОННОГО ОПРОМІНЮВАННЯ

Робота стосується дослідження випадіння преципітатів вторинної фази у бінарних і потрійних стопах на основі цирконію з низьким вмістом леґувальних елементів у межах підходу фазового поля. Розроблений модель фазового поля застосовано для вивчення випадіння преципітатів у моделю комерційних стопів Zr–Nb–Sn і Zr–Nb під час термічного оброблення. Проведено аналізу локального перегрупування леґувальних елементів і рівноважних вакансій під час випадіння преципітатів. Виконано дослідження кінетики випадіння, розмірів і розподілу преципітатів, концентрації частинок у преципітатах і матриці. Обговорено механічні властивості та пластичну деформацію у потрійному стопі з виділеними преципітатами. Показано зростання приросту межі плинности під час утворення преципітатів. Визначено межі плинности та міцности за різних швидкостей зсувної деформації відпаленого стопу. Проаналізовано утворення та ріст площин проковзування та взаємодію дислокаційних петель із преципітатами. Показано, що формування дислокаційних петель навколо преципітатів відбувається за Орованови механізмом. Проведено моделювання радіяційно-індукованого випадіння нових преципітатів під час нейтронного опромінювання цирконійових стопів з низькою концентрацією леґувальних елементів у межах розробленого моделю фазового поля з урахуванням балістичного перемішування та динаміки точкових дефектів з їхніми стоками. Показано, що в зразку, який початково містить преципітати вторинної фази, опромінення спричинює розчинення преципітатів за малих доз і випадіння нових з накопиченням дози. Виконано аналізу динаміки радіяційно-стимульованого випадіння преципітатів і статистичних розподілів преципітатів із локальним перегрупуванням нерівноважних вакансій навколо преципітатів. Показано, що конкуренція між балістичним перемішуванням і термодинамічною силою відіграє головну роль у кінетиці радіяційно-індукованого випадіння та розчинення преципітатів. Проведено оцінку механічних властивостей стопу Zr–Nb за опромінювання в реакторних умовах.

Ключові слова: фазове поле, преципітати, нейтронне опромінення, дефекти, зміцнення.